



Diverging runoff drives uncertainty in Antarctic surface mass balance projections under a high emission scenario

Benjamin Heurgue¹, Charles Amory¹, Christoph Kittel², Fredrik Boberg³, Gaël Durand¹, Vincent Favier¹, Xavier Fettweis², Quentin Glaude^{2,4}, Heiko Goelzer⁵, Nicolaj Hansen³, Nicolas C. Jourdain¹, Ruth Mottram³, Martin Olesen³, Willem Jan Van de Berg⁶, Michiel R. Van den Broeke⁶, and René R. Wijngaard⁷

¹Institut des Géosciences de l'Environnement (IGE), Univ. Grenoble Alpes/CNRS/IRD/G-INP, Grenoble, France

²Physical Geography Research Group, Department of Geography, Vrije Universiteit Brussel, Brussels, Belgium

³Department of National Centre for Climate Research (NCKF), Danish Meteorological Institute, Copenhagen, Denmark

⁴Applied Computer Electronics Laboratory, University of Liège, Liège, Belgium

⁵Norwegian Research Centre (NORCE), Bjerknes Centre for Climate Research, Bergen, Norway

⁶Institute for Marine and Atmospheric Research Utrecht, Utrecht University, Utrecht, the Netherlands

⁷Department of Physical Geography, Utrecht University, Utrecht, the Netherlands

Correspondence: Benjamin Heurgue (benjamin.heurgue@univ-grenoble-alpes.fr) and Charles Amory (charles.amory@univ-grenoble-alpes.fr)

Abstract. Three recent downscalings of CESM with MAR, RACMO, and HIRHAM under SSP5-8.5 produce consistent contemporary Antarctic surface mass balance (SMB), but diverge strongly by 2100, especially over ice shelves. HIRHAM simulates a large SMB decline driven by strong runoff increases, MAR a moderate decrease, while RACMO maintains near balance.

These differences mainly reflect contrasting melt–albedo feedbacks, present-day melt and refreezing levels, and a persistent 5 1–2 °C temperature offset between MAR and RACMO. CESM shows a decline similar in magnitude to MAR, with high melt partly compensated by extensive refreezing. Over grounded ice, all models project increased SMB from higher snowfall, though runoff still drives their spread. Despite shared boundary conditions and similar contemporary SMB, model behavior diverges, and CESM’s integrated results resemble MAR’s despite its coarse resolution. Performance differences in present-day melt suggest that uncertainty estimates should account for model skill, motivating Bayesian treatment of multi-model 10 ensembles.

1 Introduction

Antarctic ice sheet currently represents one of the largest sources of uncertainty in sea-level projections (Fox-Kemper et al., 2021), as even the sign of its net contribution by 2100 remains unclear due to the competing effects of SMB and ice-dynamical losses (Seroussi et al., 2020; Coulon et al., 2023; Edwards et al., 2021). The SMB itself represents the net effect of surface mass gains (through snowfall, rainfall and deposition of moisture and drifting snow by wind) and losses (through rain and meltwater runoff, sublimation/evaporation and erosion by wind). Antarctic ice sheet loss has already accelerated, from $-40 \pm 9 \text{ Gt yr}^{-1}$ 15 in 1979–1990 to $-252 \pm 26 \text{ Gt yr}^{-1}$ over 2009–2017 (Rignot et al., 2019; Otosaka et al., 2023), although recent observations suggest a general stalling of mass loss since 2020 (as indicated by GRACE data), which includes a temporary mass increase



observed between 2021-2024 owing to significant positive snowfall anomalies (Wang et al., 2023; Clem et al., 2023).

20

Currently the Antarctic SMB is dominated by snowfall, while runoff plays a marginal role (e.g., Agosta et al., 2019), probably subordinate to sublimation and blowing snow snow losses (Gadde and van de Berg, 2024). Recent regional climate models consistently estimate that nearly all meltwater refreezes within the snowpack during the contemporary period (e.g., Agosta et al., 2019). In a warmer future, models predict that precipitation will increase almost linearly with temperature, consistent 25 with the Clausius–Clapeyron relation, while surface melt and runoff will evolve non-linearly, notably due to the amplification induced by the melt–albedo feedback (Hofsteenge et al., 2025; Jakobs et al., 2021b; Kittel et al., 2021). Consequently, SMB over the grounded ice sheet, where melt remains small owing to low temperatures, is expected to increase until 2100 in all emission scenarios, primarily due to enhanced precipitation and only partly offset by increasing runoff, with a larger increase 30 in the warmer scenarios (Kittel et al., 2021; Boberg et al., 2022; Van Wessem et al., 2023; Jourdain et al., 2025). In contrast, SMB over the warmer ice shelves is projected to decline due to intensified surface melt and runoff, particularly under high-emission scenarios.

The climate models used to estimate the SMB of ice sheets fall into two categories: Earth system models (ESMs) and regional climate models (RCMs), each having its own strengths and limitations. The main advantage of ESMs for simulating 35 ice-sheet SMB lies in their physically consistent global framework, with interactive coupling between the atmosphere, ocean, sea ice, and land surface. However, most ESMs currently face two major limitations that constrain their ability to represent the SMB (Lenaerts et al., 2019). First, the representation of the snowpack and its interactions with the atmospheric boundary layer remains rudimentary in most models. Second, the typical horizontal resolution of the latest generation of ESMs, on the order of one degree of latitude (Eyring et al., 2016), remains insufficient to capture the steep topographic gradients and associated 40 orographic precipitation and other climate gradients that characterize the coastal margins (Herrington et al., 2022; Smith et al., 2021). A way to overcome these limitations is through dynamical downscaling, i.e., the use of a polar dedicated high-resolution RCM driven at its lateral boundaries by an ESM or by reanalysis data. RCMs provide substantially higher spatial resolution, ensuring a more comprehensive representation of SMB components, further supported by a generally more detailed description 45 of the atmospheric and surface processes typical of polar regions (Nowicki et al., 2020). Recent versions of state-of-the-art, polar-oriented RCMs show comparable skill in simulating the contemporary Antarctic SMB, with a relatively broad consensus emerging from their estimates of individual SMB components (Mottram et al., 2021). However, RCMs are not self-sufficient in terms of forcing and may introduce additional uncertainty due to potential internal biases or their climate sensitivity particularly in the context of climate projections.

50 Recent projections of Antarctic SMB up to the end of the century have been produced using the reference RCMs MAR (Kittel et al., 2021), RACMO (Van Wessem et al., 2023), and HIRHAM (Boberg et al., 2022), providing valuable insights into future SMB variability under different climatic conditions and scenarios. However, the use of different boundary conditions across these models hampers the quantification of the variability specifically attributable to the choice of RCM. To address



this gap, the present study performs an intercomparison of SMB simulated by these three RCMs, all driven by the same ESM, 55 the Community Earth System Model (CESM), under a high-emission scenario (SSP5-8.5). The ESM outputs themselves are also analyzed and compared to the RCMs. The choice of the SSP5-8.5 scenario allows us to investigate the extreme climate responses of the models under a high-end warming trajectory.

2 Climate Models and Methods

2.1 Climate Models

60 RCMs, when constrained at their lateral boundaries by an ESM, dynamically downscale atmospheric conditions to finer resolutions while explicitly resolving physical processes that are more detailed or regionally relevant than those represented in models run at the global scale. Such an approach is particularly suited for the Antarctic ice sheet, where SMB is strongly influenced by localized processes such as orographic precipitation, surface melting, or katabatic winds. In this study, we adopt this framework to evaluate the Antarctic SMB by dynamically downscaling an ESM with three RCMs: MAR, RACMO and HIRHAM. 65 In each RCM, boundary conditions are imposed every six hours at all atmospheric levels (pressure, zonal and meridional wind components, temperature, specific humidity), and at the ocean surface (sea-ice concentration and sea-surface temperature). In addition, MAR and RACMO apply an internal nudging towards driving wind and temperature fields in the upper atmosphere to ensure consistency with the large-scale circulation over the interior model domain. The models analyzed in this study are not 70 coupled to an ice-dynamics model. They therefore assume a fixed ice-sheet geometry (topography and extent), which excludes both melt–elevation feedback and the effects of topographic changes on atmospheric circulation (Delhasse et al., 2024).

This subsection provides a concise description of each of the four models used in this study, along with a comparative 75 summary of parameterizations involved in representing melt and the treatment of liquid water within the snowpack. It is also important to note that only RACMO, among the model versions employed here, includes snow transport by wind in the computation of SMB. Since runoff rapidly becomes the dominant component of surface ablation in Antarctica (by at least one order of magnitude compared to other ablation terms; Kittel et al., 2021) in a warmer climate, and because wind-driven snow erosion is supposed to interact only locally with the other SMB components (Lenaerts and van den Broeke, 2012), the omission of this process is not expected to compromise our intercomparison. In particular, under warmer conditions, the increased occurrence of surface liquid water further limits blowing snow (Li and Pomeroy, 1997). From here on, this difference 80 will not be repeatedly mentioned, so as to focus solely on processes related to surface and snowpack water content (melt, rainfall, percolation, retention, refreezing, and runoff). The main model features relevant to resolving these processes are listed in Table 1. The specific model versions are detailed in each paragraph.



2.1.1 CESM2.1

The Community Earth System Model version 2.1 (CESM) is a global climate model from the CMIP6 generation Danabasoglu et al. (2020), developed by the National Center for Atmospheric Research (NCAR). It interactively integrates the atmosphere (Gettelman, 2019), ocean and sea ice (Hunke and Lipscomb, 2010), and land surface components (Lawrence et al., 2019), with a nominal horizontal resolution of 1-degree (≈ 110 km) finite volume grid (f09_g16). Its land surface component incorporates an advanced representation of snowpack processes (van Kampenhout et al., 2017), with a 12-layer stratification spanning a firm column with 10 m water equivalents (WE) (Lawrence et al., 2019; van Kampenhout et al., 2020). Snow albedo is computed across five spectral bands in the visible and in the near-infrared and primarily depends on grain size, density, and the presence of impurities (Flanner and Zender, 2005; Flanner et al., 2007). Finally, firn is initialized through a long spin-up, allowing the model to reach a quasi-steady state of densification, percolation/refreezing, and grain-size evolution consistent with the imposed climate forcing (van Kampenhout et al., 2017).

In this study, we use a CESM member specifically produced at Utrecht University (van Kampenhout et al., 2020), which was branched in 1950 from the CMIP6 historical simulation and follows the CMIP6 experimental protocol. This member is not part of the official CMIP6 ensemble but was generated to provide the 6-hourly three-dimensional atmospheric fields required to drive RCMs at their lateral and surface boundaries, at a time when the official CESM2 runs for CMIP6 at NCAR did not archive variables at this temporal resolution.

100

CESM was selected as the common forcing for the three RCMs for several reasons. First, it was among the first CMIP6 ESMs to provide high-frequency (6-hourly) atmospheric forcing data both at the surface and throughout the entire atmospheric column (3D), required for driving RCMs at their boundaries. In addition, CESM has emerged as one of the best-performing models in an intercomparison exercise assessing the ability of CMIP6 ESMs to simultaneously represent contemporary climate at both poles (Agosta et al., 2022). Finally, the level of detail in its land-surface scheme, through coupling with the Community Land Model version 5 (CLM5), allows for an advanced representation of the SMB components, including snow accumulation, melt, refreezing, and runoff (van Kampenhout et al., 2017; Lawrence et al., 2019; Dunmire et al., 2022). This detailed representation of the various SMB components makes CESM outputs directly comparable with those of the RCMs, enabling a consistent intercomparison.

110 2.1.2 RACMO 2.3p2

The Regional Atmospheric Climate Model (RACMO) is developed by the Royal Netherlands Meteorological Institute (KNMI), with its polar component primarily maintained at the Institute for Marine and Atmospheric Research Utrecht (IMAU). The simulations analyzed in this study are based on the Antarctic runs of RACMO2.3p2 at 27 km horizontal resolution (Van Wessem et al., 2018). For simplicity, this version is hereafter referred to as RACMO. It has been widely used to simulate the climate of the Greenland (Noël et al., 2018) and Antarctic (Van Wessem et al., 2018) ice sheets. RACMO combines the hydrostatic



dynamical core of the HIRLAM model with the CY33r1 physics package of the European Centre for Medium-Range Weather Forecasts (ECMWF). Its snow scheme represents a maximum of 100 layers, but in practice it varies around 35–50 layers (typically 35 for ablation areas and up to 50 for high accumulation areas after long runs), discretized over a depth of at least 30 m. In RACMO, snow albedo is calculated through a prognostic scheme for snow grain size, modulated by cloud cover and 120 solar zenith angle (Munneke et al., 2011). The firn column is initialized using climatological profiles of temperature, density, and liquid water content derived from the IMAU Firn Densification Model (IMAU-FDM) (Ligtenberg et al., 2011). The model employs topographic data from Cook et al. (2012) and Bamber et al. (2009).

2.1.3 MARv3.11

The Regional Atmospheric Model (MAR) is mainly developed at the University of Liège in Belgium. The version of the model 125 employed in this study is MARv3.11, specifically developed for Antarctica and run at a horizontal resolution of 35 km (Agosta et al., 2019). For simplicity, this version is hereafter referred to as MAR. It has been widely used to simulate the climate in high latitudes, including Antarctica (e.g., Kittel et al., 2021) and Greenland (e.g., Fettweis et al., 2017). The atmospheric dynamics of MAR are based on the hydrostatic approximation of the primitive equations (Gallée and Schayes, 1994), while 130 its microphysics scheme employs prognostic equations for five water species: specific humidity, cloud droplets, ice crystals, raindrops, and snow particles (Gallée, 1995). Its snow scheme represents 30 layers (with time varying thickness) discretized over a depth of 20 m. MAR dynamically computes surface albedo based on snow properties (grain size, density), zenithal angle as well as cloud cover (Tedesco et al., 2016). The snowpack is initialized with zero liquid water content, temperature and density profiles from a prior simulation over the contemporary period, followed by a spin-up phase, corresponding to the 135 initialization time required for the model to reach a thermodynamic equilibrium between the surface and atmosphere consistent with its boundary conditions. The topography used in MAR is derived from the Bedmap2 surface elevation dataset (Fretwell et al., 2013).

2.1.4 HIRHAM5

The regional climate model HIRHAM (Christensen et al., 2007) results from the combination of the numerical weather prediction model HIRLAM7 (Eerola, 2006) and the hydrostatic general circulation model ECHAM5 (Roeckner et al., 2003). This 140 model has been developed through a collaboration between the Danish Climate Centre of the DMI (Danish Meteorological Institute) and the Alfred Wegener Institute (AWI), Helmholtz Centre for Polar and Marine Research. The simulations analyzed in this study are based on HIRHAM5, hereafter referred to simply as HIRHAM, which has been optimized to represent the Greenland climate and run in Antarctica at a horizontal resolution of 12.5 km (Boberg et al., 2022). While HIRHAM does include a surface energy and mass budget scheme over ice sheets, it has few (5) widely spaced layers and the results presented 145 here are therefore from an offline SMB model. This means that the surface scheme is forced by atmospheric outputs but does not feed back on the atmosphere during the simulation. The snowpack thickness is 60 m water equivalent (WE), subdivided into 32 layers, and firn density evolves under overburden pressure using established compaction schemes (Langen et al., 2017). In HIRHAM5, surface albedo is a linear function of surface temperature, with a minimum value of 0.65 at the melting point and



a maximum value of 0.85 for surface temperatures of -5°C and below (Lucas-Picher et al., 2012). Albedo is also influenced
150 by cloud cover and the solar zenith angle. The snowpack is initialized through a 50-year spin-up, based on a prescribed profile derived from historical simulations. At the start of the spin-up, the deep temperature in the bottom layer is initialised as the mean annual temperature from the RCM's first 10 years. This decadal time series is repeated offline until the snowpack reaches equilibrium. It is then used as a starting condition in the HIRHAM model as it is run into the future. Liquid water (melt and rain) percolate into the snow and refreeze according to the cold content of the layers, the mass of which is tracked using an
155 Eulerian scheme. Full details are given in Hansen et al. (2024); Langen et al. (2017). The topography used in HIRHAM is derived from the GTOPO30 surface elevation dataset (Mottram et al., 2021).

2.2 Comparative analysis of parameterizations

When comparing projections from the different models, it is crucial to consider the specific parameterizations implemented in each RCM (Table 1). One key difference lies in how atmosphere–surface interactions are handled: HIRHAM operates
160 with a decoupled atmosphere–surface setup, whereas MAR, RACMO, and CESM employ fully interactive coupling, allowing feedbacks from the surface to influence the atmosphere. The models also differ in the initialization of their snow and firn schemes, and all use a different spin-up method. Total snowpack thickness ranges from 20 m in MAR to 62 mWE in HIRHAM, when it is variable in RACMO and set to 10 mWE in CESM, while the vertical layering varies in both number and thickness of layers in the four models. Percolation—the downward movement of liquid water within the snowpack—is represented in
165 MAR, RACMO and CESM using a bucket-type approach: once a layer reaches its maximum water retention capacity (also known as irreducible water saturation), excess water is passed to the layer below, and any remaining water that is not retained in the firn or refrozen within the current time step contributes to runoff. In all four models, runoff is treated as a purely vertical process and does not account for lateral water fluxes. HIRHAM follows a more physical approach in which the vertical flow of liquid water is governed by a Darcy's law (Langen et al., 2017). In any of these strategies, the efficiency of the percolation process depends on the water retention capacity, defined as a percentage of the available pore space of each layer, which
170 differs between models from a fixed 2% in RACMO to a maximum set to 7% per layer in HIRHAM (Machguth et al., 2024). Albedo specifications for fresh snow and bare ice also vary across models, directly affecting the strength of the melt–albedo feedback. Lower albedo values, for instance, enhance melt through increased absorption of solar radiation. These parametric and structural differences are important sources of variability in ice sheet surface mass balance projections, as highlighted in
175 previous comparative studies over Antarctica (Mottram et al., 2021) and Greenland (Fettweis et al., 2020; Glaude et al., 2024).



Table 1. Comparison of the main characteristics and parameterizations of the climate models

	RACMO 2.3p2¹	MARv3.11²	HIRHAM5³	CESM2⁴
Horizontal resolution	27 km	35 km	12.5 km	(1°) 110 km
Firn thickness	≥30 m	20 m	62 m WE ⁵	10 m WE ⁷
Number of firn layers	35–50	30	32 ⁵	12 ⁷
Albedo	fresh snow: 0.85, bare ice: 0.55	fresh snow: 0.94, bare ice: 0.55	fresh snow: 0.85, bare ice: 0.4 ⁵	fresh snow: 0.85, bare ice: 0.5 ⁷
Maximum water capacity	2%	5%	7% ⁶	3.3%

¹Van Wessem et al. (2018); ²Kittel et al. (2021); ³Boberg et al. (2019); ⁴Danabasoglu et al. (2020); ⁵Hansen et al. (2021); ⁶Langen et al. (2017); ⁷van Kampenhout et al. (2017)

2.3 Intercomparison protocol

For the purpose of inter-model comparison, all outputs from the four models were bi-linearly interpolated onto a common 10 km regular stereographic polar grid (EPSG3031), which differs from the native grids of each model. This grid has been adopted from the Ice-sheet Model Intercomparison Project phase 6 (ISMIP6) (Seroussi et al., 2020). A common ice mask, defined as the maximum ice extent common to the four models, was also applied to ensure comparisons over identical areas, as previous studies demonstrate that considering different ice masks can have a major impact on SMB results (Hansen et al., 2022). The digital elevation model used to generate model topography on each model's native grid differs among the four models (Sect. 2.1). This leads to differences in surface elevation between models. While RCMs generally show good agreement with differences most pronounced in areas of steep topographic gradients, CESM generally features higher elevations over ice shelves and lower elevations over grounded ice (Fig. S1 in the Supplement). The 1995–2014 period was chosen as the 20-year contemporary reference, during which Antarctic SMB remained relatively stable (Mottram et al., 2021), in line with ISMIP6 recommendations (Seroussi et al., 2020).

In order to compare the four models on an equal footing, the analysis is primarily conducted in terms of anomalies with respect to their own present day climate. We refer to future anomalies—as the difference between the mean of the 2080–2099 period and that of the reference period 1995–2014, and into-time series anomalies—as the deviation of each annual value



from this same reference mean. This approach highlights projected trajectories while minimizing the influence of systematic biases that may arise from parametric and structural differences between the models and the resulting representation of the contemporary climate. Furthermore, by defining the reference period as representative of a stable climate (Mottram et al., 195 2021), each model can establish its own equilibrium state, particularly with respect to the surface energy balance. However, differences in this initial equilibrium affect both the magnitude and direction of projected long-term anomalies. Therefore, to identify the mechanisms underlying inter-model discrepancies, this anomaly-based analysis is complemented by an evaluation in absolute values.

3 Results

200 In this result section we first compare RCM simulations driven by CESM and ERA5, assess inter-model differences regardless of the chosen forcing over the contemporary period, and evaluate modeled melt days against satellite observations (Sec. 3.1). Second, we examine SMB projections and their individual components to identify the main contributors to inter-model variability (Sec. 3.2). Finally, we provide a detailed analysis of these components to determine the drivers of SMB variability projected by the end of the century (Sec. 3.3).

205 **3.1 Evaluation**

3.1.1 Evaluation of dynamical downscalings over the contemporary period

Before analyzing projections, it is essential to assess the ability of the three RCMs driven by CESM to reproduce a realistic SMB over the contemporary period. To this end, we compare their dynamical downscalings of CESM to their respective reference versions driven by ERA5 over the 1995–2014 reference period, all interpolated to a common grid of 10 km resolution. 210 Table 2 shows that integrated SMB estimates over the common ice mask are very close between the two forcings for each RCM, with differences of 38, 51, and 30 Gt yr⁻¹ for HIRHAM, MAR, and RACMO, respectively. These differences are well below the interannual variability (standard deviation over the period) by factors between 1.7 and 3. Confirming that CESM downscalings are in good agreement with the ERA5-driven reference simulations. Figure 1 illustrates the spatial SMB 215 differences between CESM- and ERA5-driven simulations, with hatching indicating areas where differences are smaller than or equal to the interannual SMB variability in the ERA5-driven simulations. A consistent spatial pattern of deviations is observed across the three RCMs, suggesting that the differences mainly originate from the CESM forcing itself, linked to distinct atmospheric circulation regimes between CESM and ERA5, rather than the RCM used. For example, as shown in Fig. 1, CESM-driven RCMs overestimate SMB in the region spanning from the Antarctic Peninsula through Queen Maud Land to the Amery Ice Shelf, a direct consequence of CESM's overestimation of precipitable water and sea-level pressure in this area 220 (Kittel et al., 2021). Underestimation is also observed in Wilkes Land and the periphery of West Antarctica. While strong performance under present-day conditions does not necessarily guarantee accurate projections, it is a necessary prerequisite.



These results therefore support the use of CESM downscalings as sufficiently reliable for the analysis of climate projections presented in the remainder of this study.

Table 2. Integrated values over the contemporary period (1995–2014) of SMB, precipitation (PR), runoff (RU), melt (ME), and refreezing (RF), integrated over the entire Antarctic ice sheet in Gt yr^{-1} for the three models driven by CESM and ERA5.

Forcing	Models	SMB	PR	RU	ME	RF
CESM	HIRHAM	2473 ± 130	2786 ± 138	124 ± 17	456 ± 60	332 ± 58
	MAR	2612 ± 113	2770 ± 111	16 ± 4	88 ± 14	85 ± 13
	RACMO	2432 ± 123	2604 ± 123	2 ± 2	89 ± 19	87 ± 18
ERA5	HIRHAM	2435 ± 93	2752 ± 89	132 ± 26	500 ± 100	368 ± 89
	MAR	2561 ± 85	2757 ± 83	36 ± 12	130 ± 31	107 ± 23
	RACMO	2462 ± 91	2673 ± 90	1 ± 1	92 ± 22	91 ± 22

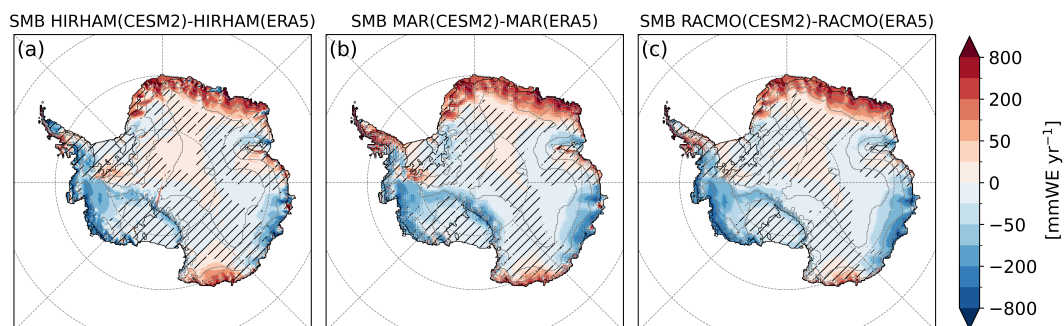


Figure 1. Differences in mean Antarctic SMB simulated by the RCMs: HIRHAM (a), MAR (b), and RACMO (c), driven by CESM and ERA5, in mmWE yr^{-1} , over the reference period 1995–2014. Hatched areas indicate regions where the differences are smaller than the interannual variability (standard deviation over the period) of the SMB from RCMs driven by ERA5.

Although the integrated SMB values are quite close across the models (with differences between 2% and 7%), their individual components (Table 2) reveal pronounced inter-model differences that appear largely independent of the forcing used. In particular, HIRHAM consistently produces substantially higher melt rates and runoff than MAR and RACMO over the present day period, in line with previous assessment of HIRHAM when driven by reanalysis (Boberg et al., 2022). For instance, HIRHAM simulates melt rates approximately five times greater than those of the other two RCMs, accompanied by refreezing about four times higher than in MAR and RACMO. This refreezing partially suppresses melt, yet significant runoff still occurs, amounting to $124 \pm 17 \text{ Gt yr}^{-1}$ for CESM-driven HIRHAM and $132 \pm 26 \text{ Gt yr}^{-1}$ for ERA5-driven HIRHAM, compared with only $16 \pm 4 \text{ Gt yr}^{-1}$ and $36 \pm 12 \text{ Gt yr}^{-1}$ for MAR, and $2 \pm 2 \text{ Gt yr}^{-1}$ and $1 \pm 1 \text{ Gt yr}^{-1}$ for RACMO. The



similarity of these magnitudes between the two forcings for a given RCM clearly indicates that these differences arise from the intrinsic regional model physics rather than the atmospheric forcing. This is particularly important given that the temperature–melt relationship is non-linear due to the positive melt–albedo feedback. This is particularly important given that the
235 temperature–melt relationship is non-linear due to the positive melt–albedo feedback. These results suggest that in HIRHAM the firn layer loses its meltwater retention capacity more rapidly, promoting runoff in response to an increase in surface liquid water.

3.1.2 Evaluation of RCMs melt days

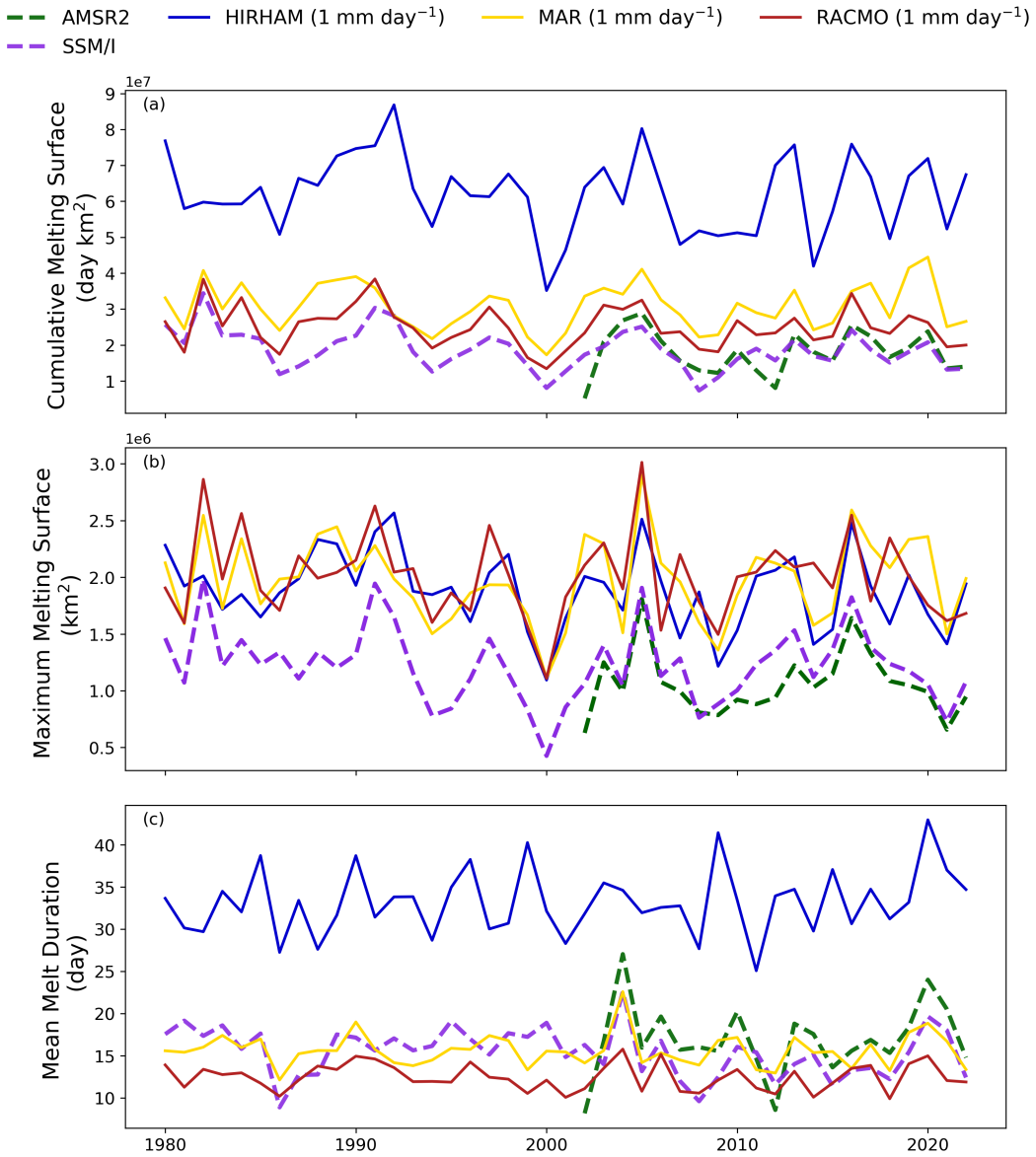


Figure 2. Annual time series (calendar years) of the Cumulative Melting Surface (CMS; day km²) (a), the Maximum Melting Surface (MMS; km²) (b) and the Mean Melt Duration (MMD; day) (c) during the period 1980–2022. For the models MAR (yellow), HIRHAM (blue), and RACMO (red), driven by ERA5 at thresholds of 1 mm day⁻¹. For the satellite observations AMSR2 (green, dashed line) and SSM/I (purple, dashed line).



Each RCM has already been individually and extensively evaluated against SMB and near-surface meteorological observations
240 (e.g., Kittel et al., 2021; Van Wessem et al., 2018; Mottram et al., 2021). However, to assess the ability of the three RCMs to represent surface melt within our intercomparison protocol, we compare the simulated number of surface melt days—defined using a threshold of 1 mm day^{-1} as in Donat-Magnin et al. (2020), owing to the strong sensitivity of microwave signals to surface meltwater (Picard et al., 2022)—with satellite observations from the Advanced Microwave Scanning Radiometer 2 (AMSR2) and the Special Sensor Microwave/Imager (SSM/I). These satellite sensors allow the detection of liquid water at or
245 close to the snowpack surface. The satellite data were regridded to the ISMIP6 10 km grid and the daily RCM outputs used for this comparison originate from a dynamical downscaling of ERA5.

Figure 2 shows the Cumulative Melting Surface (CMS; day km^2) (Fig. 2a), the Maximum Melting Surface (MMS; km^2) (Fig. 2b) and the Mean Melt Duration (MMD; day) (Fig. 2c), all defined in (Torinesi et al., 2003). CMS represents the spatial
250 yearly (calendar year) sum of melt days multiplied by the pixel area ($10 \times 10 \text{ km}^2$). The MMS corresponds to the surface over which melting is detected at least once during the corresponding year, and the MMD is calculated by dividing the CMS by the MMS. For the threshold of 1 mm day^{-1} , both MAR and RACMO show good agreement with the observations, with a Normalized Root Mean Square Error (NRMSE, Eq. S1 in the Supplement) on MMD of 15% and 21% when compared with SSM/I, and 17% and 32% with AMSR2. In contrast, HIRHAM presents significantly more mean melt days, with an NRMSE
255 of 135% and 104% for SSM/I and AMSR2, respectively. Note that for HIRHAM the statistics show little sensitivity to the choice of the daily threshold compared to MAR and RACMO, owing to its much higher melt rates. For HIRHAM, increasing the threshold up to 3 mm day^{-1} has only a limited impact on MMD with a NRMSE decrease at 108% compared to SSM/I (a threshold close to 10 mm day^{-1} is required to bring HIRHAM closer to the observations). By contrast, for MAR and RACMO, a 3 mm day^{-1} threshold leads to an increase in the MMD NRMSE at 34% and 46%, respectively, relative to AMSR2.

260
On Figure 2b, MMS shows that HIRHAM produces melt over surfaces of similar extent to those of MAR and RACMO (ranging between $2.0 \times 10^6 \text{ km}^2$ and $1.8 \times 10^6 \text{ km}^2$ for the models), which are all above the observed melting surface ($1.1 \times 10^6 \text{ km}^2$ and $1.2 \times 10^6 \text{ km}^2$ for AMSR2 and SSM/I; Table 3). We can also note the fact that for HIRHAM, the difference in the threshold does not significantly impact the total extent of the melting surface. This figure highlights several points: first, MAR and
265 RACMO faithfully represent the observations, confirming previous findings regarding surface melting (e.g. Kuipers Munneke et al., 2012; Kittel et al., 2021; Van Wessem et al., 2023). Second, HIRHAM produces significantly more melt over approximately the same melting areas, which is attributed to its high melt rates. This discrepancy is reflected in the MMD (Fig. 2c), where HIRHAM simulates an average melt duration of 33.7 ± 4.0 days across the melting area, compared to 16.8 ± 4.3 and 14.5 ± 3.0 days for AMSR2 and SSM/I, respectively (Table 3). This confirms that the major deviation in CMS results from the
270 model sustaining melt for a longer average period even with high melt rates threshold.



Table 3. Means values of Cumulative Melting Surface (CMS; day km^2), Maximum Melting Surface (MMS; km^2) and Mean Melting Duration (MMD; day) over the period (1980–2022) for HIRHAM, MAR, RACMO and SSM/I and over (2002–2022) for AMSR2. The threshold of 1 mm day^{-1} is used for models. The standard deviation represents the interannual variability.

	CMS ($\times 10^6$ day km^2)	MMS ($\times 10^6 \text{ km}^2$)	MMD (day)
HIRHAM	61.2 ± 10.9	1.8 ± 0.3	33.7 ± 4.0
MAR	31.5 ± 6.3	2.0 ± 0.4	15.6 ± 2.3
RACMO	24.8 ± 4.5	2.0 ± 0.4	12.4 ± 1.8
AMSR2	17.9 ± 6.1	1.1 ± 0.3	16.8 ± 4.3
SSM/I	17.4 ± 4.3	1.2 ± 0.3	14.5 ± 3.0

3.2 Inter-model comparison of SMB projections

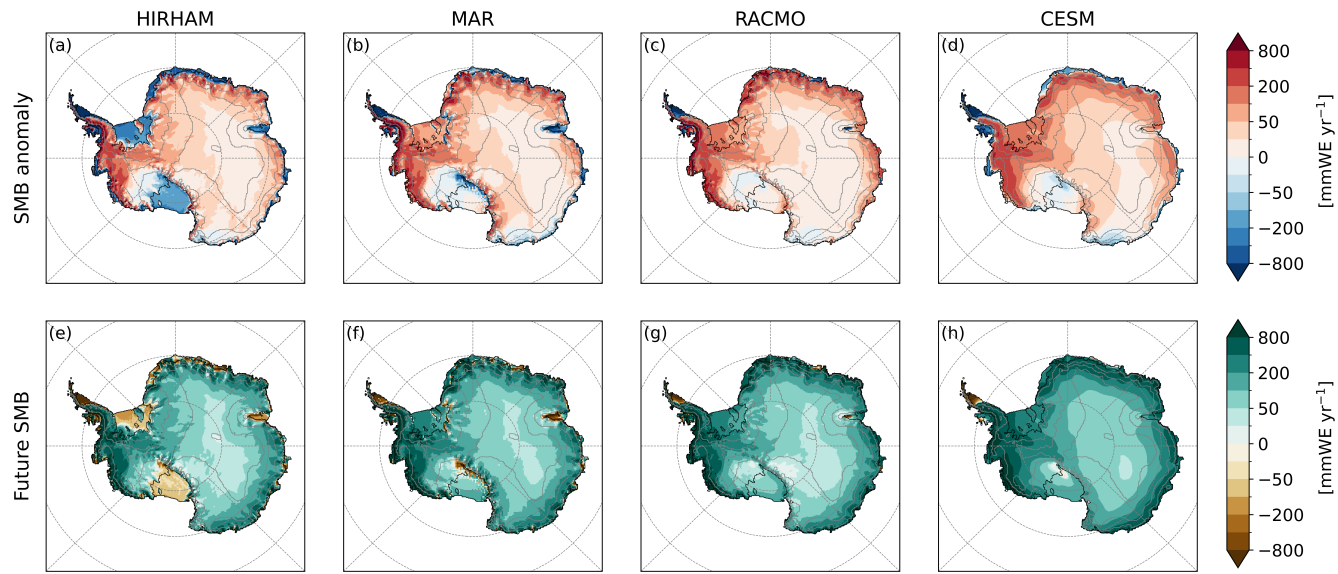


Figure 3. SMB anomaly between the means of 2080–2099 and 1995–2014; HIRHAM (a), MAR (b), RACMO (c) and CESM (d) and mean future SMB over 2080–2099; HIRHAM (e), MAR (f), RACMO (g) and CESM (h), in mmWE yr^{-1} , under the SSP5-8.5 scenario.

Figure 3 shows SMB future anomalies over the entire Antarctic Ice Sheet for the period 2080–2099 relative to 1995–2014, expressed in mmWE yr^{-1} (Fig. 3a–d). All four models—HIRHAM (Fig. 3a), MAR (Fig. 3b), RACMO (Fig. 3c), and CESM (Fig. 3d)—show a clear contrast between the grounded ice sheet, characterized by increased SMB (positive anomalies), and the floating ice shelves, which mostly experience a decline in SMB (negative anomalies). In HIRHAM, all ice shelves exhibit



negative anomalies. MAR simulates a more localized decrease, notably over the Amery ice shelf, along the ice shelves of Queen Maud Land and over Larsen ice shelf. RACMO shows relatively stable SMB across most ice shelves, close to present-day equilibrium, except over Larsen ice shelf and a few shelves in Queen Maud Land, where negative anomalies also appear. In CESM, negative anomalies are primarily observed over the Antarctic Peninsula and along the ice shelves of Queen Maud 280 Land. In MAR, RACMO, and CESM, the large Ronne–Filchner and Ross ice shelves maintain generally positive anomalies. In addition, MAR shows negative SMB values along parts of the grounding lines of the Ross and Ronne–Filchner ice shelves. These localized deficits are very likely related to interactions between the local atmospheric circulation and the Transantarctic Mountains, including foehn-induced or adiabatic warming, as well as enhanced snowfall sublimation (Agosta et al., 2019). Over the grounded ice sheet, all four models consistently indicate a general increase in SMB, with similar spatial patterns: 285 stability over the Antarctic Plateau and a pronounced increase in the western part of the ice sheet.

Future means for the period 2080–2099 (Fig. 3d–f) confirm these trends, with enhanced ablation in HIRHAM, where most ice shelves exhibit negative SMB. In MAR and RACMO, negative values are primarily confined to the Antarctic Peninsula and the Amery Ice Shelf. In CESM, only the tip of the Antarctic Peninsula shows negative SMB. Moreover, relative to the RCMs, 290 CESM reproduces a relatively latitudinally homogeneous field with high values, dominated by a coast-to-plateau gradient. This pattern directly reflects the limited horizontal resolution, which controls the representation of topographic gradients and influences orographic precipitation in the model, particularly visible along the margins of Queen Maud Land, in West Antarctica, and around the Amery Ice Shelf.

295 Given this pronounced distinction between grounded and floating regions, and to avoid obscuring their divergent SMB trajectories, we choose to analyze them separately for the remainder of the study.

Under warmer conditions, the continent-scale SMB is primarily governed by precipitation (the main accumulation component at the surface) and runoff (the main ablation component); sublimation, although locally significant, remains relatively 300 minor at the continental scale (Kittel et al., 2021). Figure 4 shows the temporal evolution of SMB, precipitation, and runoff anomalies integrated over the grounded ice and the ice shelves. These time series highlight inter-model consistency over the grounded ice, but pronounced differences on the ice shelves by 2100.

Over the grounded ice sheet, the models consistently project an increase in SMB by the end of the century (Fig. 4a), 305 with future anomalies for 2080–2099 ranging from $+610 \pm 69 \text{ Gt yr}^{-1}$ for HIRHAM to $+870 \pm 93 \text{ Gt yr}^{-1}$ for RACMO (Table 4). Despite differences in runoff (Fig. 4e), SMB is largely dominated by precipitation, with anomalies ranging from $+974 \pm 111 \text{ Gt yr}^{-1}$ for MAR to $+1171 \pm 122 \text{ Gt yr}^{-1}$ for HIRHAM (Table 4).

In contrast, projections for the ice shelves reveal substantial divergence (Fig. 4b). RACMO simulates a nearly stable SMB, 310 close to present-day equilibrium, with an anomaly of $+25 \pm 19 \text{ Gt yr}^{-1}$, resulting from a near balance between runoff



($+170 \pm 37 \text{ Gt yr}^{-1}$) and precipitation ($+203 \pm 23 \text{ Gt yr}^{-1}$, Table 4). Conversely, HIRHAM, MAR and CESM indicate net surface mass loss, with anomalies of $-529 \pm 72 \text{ Gt yr}^{-1}$, $-209 \pm 58 \text{ Gt yr}^{-1}$, and $-118 \pm 36 \text{ Gt yr}^{-1}$, respectively. These losses result from increased runoff that is no longer compensated by precipitation: runoff anomalies reach $+775 \pm 160 \text{ Gt yr}^{-1}$ for HIRHAM, $+390 \pm 76 \text{ Gt yr}^{-1}$ for MAR, and $+329 \pm 59 \text{ Gt yr}^{-1}$ for CESM. Such intermodel spread is striking at the end
315 of the century, with HIRHAM exhibiting the highest runoff rates of about 4.6 times those of RACMO, which is the model that has the most constant SMB.

These contrasts reflect not only differences in runoff magnitude but also in the timing of negative anomalies emergence: HIRHAM anticipates a transition to negative SMB anomalies as early as 2040, whereas it appears only around 2060 for MAR
320 and 2070 for CESM. Thus, inter-model dispersion over the ice shelves largely stems from the representation of runoff, in both its intensity and temporal evolution. To reduce dependence on emission scenario timing, the following analysis considers SMB component evolution as a function of the climate response rather than absolute time.

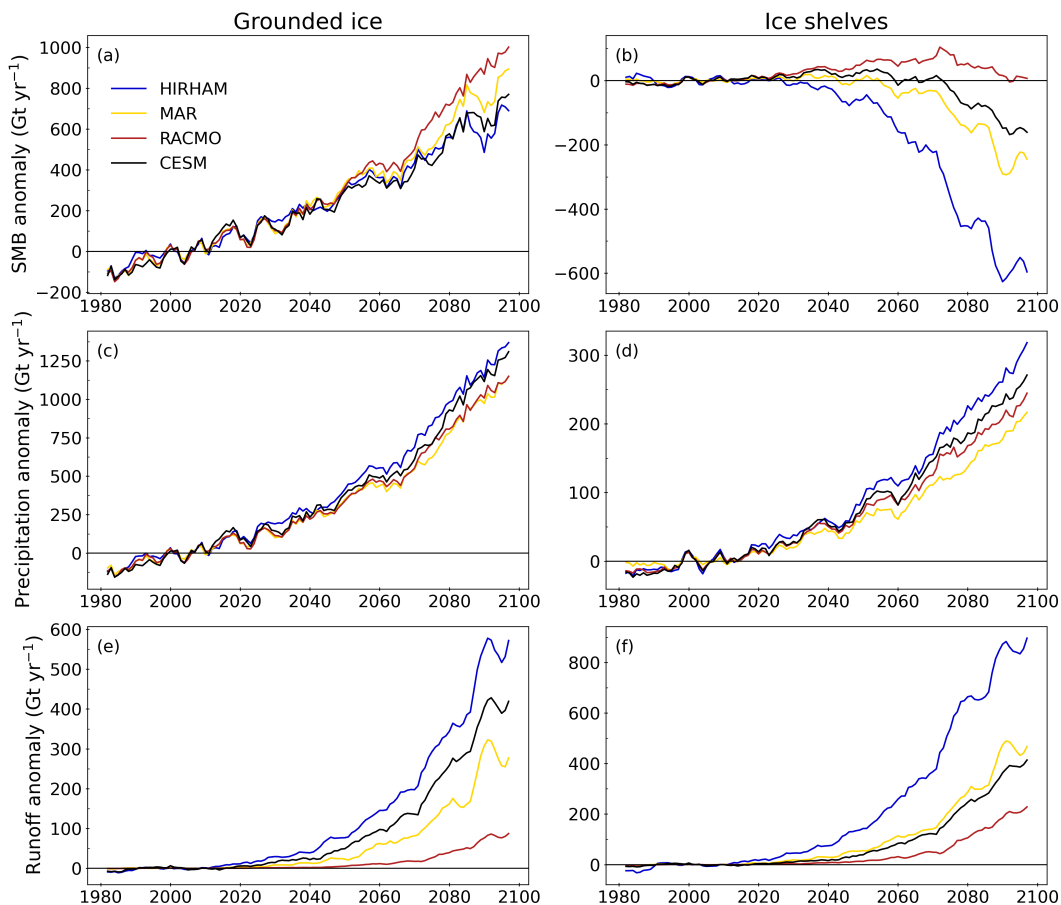


Figure 4. Time series anomalies of SMB (a, b), precipitation (c, d), and runoff (e, f), in Gt yr^{-1} , relative to the reference period 1995–2014. For the models MAR (yellow), HIRHAM (blue), and RACMO (red), driven by CESM (black) under the SSP5-8.5 scenario. Values are integrated over the grounded (left) and floating (right) parts of the ice sheet. Note that the Y-axis scales differ between grounded and floating ice due to the difference in surface areas. A 5-year running mean is applied for clarity.



Table 4. Future integrated anomalies of SMB, solid (SP) and liquid precipitation (LP), runoff (RU), melt (ME), refreezing (RF), and sublimation (SU), calculated as the mean for 2080–2099 relative to the reference period 1995–2014, in Gt yr⁻¹. For HIRHAM, MAR, and RACMO driven by CESM and CESM under the SSP5-8.5 scenario, over the grounded ice and ice shelves. The standard deviations (\pm) indicate high confidence that the integrated anomalies are all statistically different from zero. All anomalies exceed interannual variability (i.e., the standard deviation) and are therefore considered significant.

Models	SMB	SP	LP	RU	ME	RF	SU
Grounded ice (11.98×10^6 km ²)							
HIRHAM	610 \pm 69	1082 \pm 105	83 \pm 17	470 \pm 88	795 \pm 133	409 \pm 64	91 \pm 12
MAR	757 \pm 85	897 \pm 92	77 \pm 16	232 \pm 62	408 \pm 94	253 \pm 48	-15 \pm 5
RACMO	870 \pm 93	962 \pm 99	27 \pm 7	64 \pm 17	258 \pm 55	221 \pm 47	56 \pm 6
CESM	657 \pm 80	972 \pm 98	143 \pm 20	349 \pm 62	621 \pm 104	415 \pm 61	110 \pm 12
Ice shelves (1.49×10^6 km ²)							
HIRHAM	-529 \pm 72	183 \pm 17	78 \pm 15	775 \pm 94	903 \pm 89	206 \pm 14	15 \pm 1
MAR	-209 \pm 58	110 \pm 13	66 \pm 12	390 \pm 76	584 \pm 82	261 \pm 21	-4 \pm 2
RACMO	25 \pm 19	170 \pm 16	33 \pm 7	170 \pm 37	413 \pm 57	276 \pm 32	8 \pm 1
CESM	-118 \pm 36	92 \pm 10	134 \pm 17	329 \pm 59	675 \pm 86	480 \pm 45	15 \pm 2

3.3 Processes driving inter-model differences in SMB projections

Under warmer conditions, several mechanisms can enhance both the frequency and magnitude of surface runoff over the ice sheet: increased rainfall, greater liquid-water production driven by cloud-emitted longwave radiation (e.g., Kittel et al., 2022) and by the melt–albedo feedback, and a diminished water-retention capacity of the firn. Figure 5 presents annual (calendar year) near-surface air temperatures for the four models, highlighting persistent differences of 2–3 °C over both grounded ice and ice shelves. Given the strong temperature dependence of surface melt and the inter-model differences in near-surface temperature, the following results are discussed in terms of absolute near-surface temperature (note that these discrepancies are only negligibly affected by differences in topography; see Fig. S2). This approach allows us to account for the structural differences between models and to highlight their present-day states, rather than focusing solely on their temporal evolution. Moreover, to make the discussion clearer, and since the observed differences are driven by distinct physical mechanisms, we focus first on HIRHAM’s evolution, before considering how MAR, RACMO, and CESM diverge from one another.

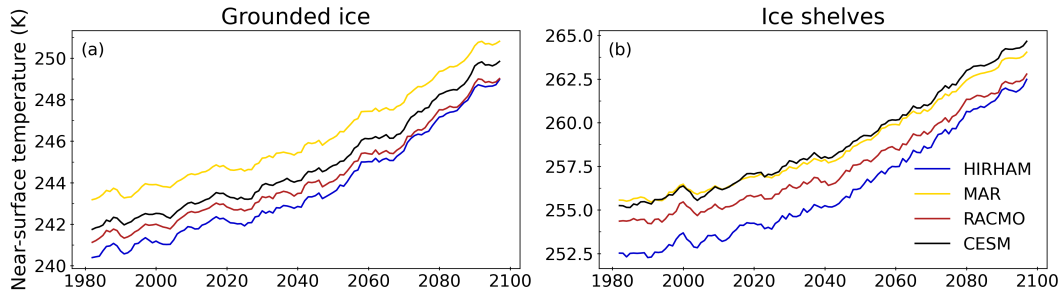


Figure 5. Time series of near-surface temperature, in K. For the models MAR (yellow), HIRHAM (blue), and RACMO (red) driven by CESM (black) under the SSP5-8.5 scenario. Values are integrated over grounded (left) and floating (right) parts of the ice sheet. Note that the Y-axis scales differ between grounded and floating ice due to the difference in surface areas. A 5-year running mean is applied for clarity.

The melt–albedo feedback is known to be a key driver of melt rate evolution and a strongly nonlinear process (e.g. Jakobs 335 et al., 2021a). Albedo directly controls the net shortwave radiation (SWN); hence, SWN anomalies are used here to represent albedo changes. Focusing first on the ice shelves, HIRHAM projects the strongest increase in SWN by the end of the simulation $+6.76 \pm 0.41 \text{ mmWE yr}^{-1}$, compared to $+0.32 \pm 0.11 \text{ mmWE yr}^{-1}$ for MAR, $+0.68 \pm 0.22 \text{ mmWE yr}^{-1}$ for RACMO, and $+1.27 \pm 0.18 \text{ mmWE yr}^{-1}$ for CESM (Fig. 6b). This pronounced anomaly in HIRHAM clearly indicates that the melt–albedo feedback strongly amplifies simulated melt rates.

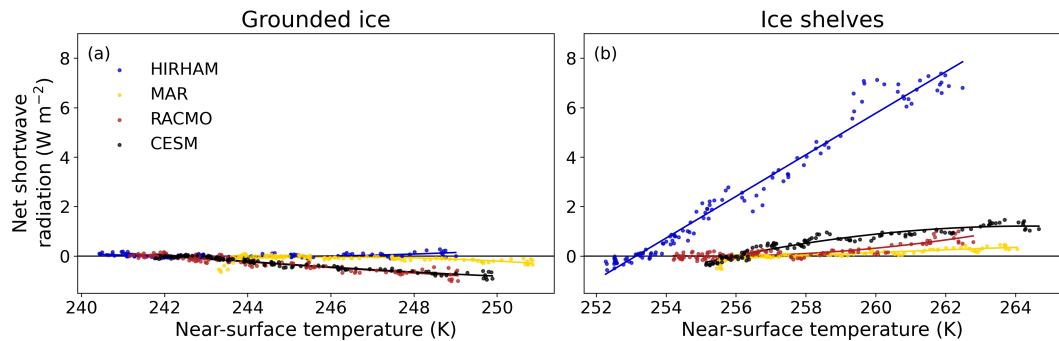


Figure 6. Net shortwave radiation (SWN), in mmWE yr^{-1} as function of the absolute annual near-surface air temperature in K. For the models MAR (yellow), HIRHAM (blue), and RACMO (red) driven by CESM (black) under the SSP5-8.5 scenario. Mean values over grounded (left) and floating (right) parts of the ice sheet. A 5-year running mean is applied for clarity.

The runaway of this positive feedback can be linked to HIRHAM's already elevated contemporary melt and refreezing. 340 HIRHAM melt and refreezing exceeds by factors of 5 and 4 from those of MAR and RACMO, and by factors of 3 and 2 from those of CESM over the ice shelves, based on mean values for the period 1995–2014 (Table S1). Moreover, because HIRHAM starts from slightly lower temperatures, when we compare its melt and refreezing rates with those at the starting temperatures of MAR, RACMO, and CESM (255–256 K), its rates already match those projected at the end of the simulation under a high-



345 emission scenario (Fig. 7b, d). The combination of early high melt rates and distinct SWN evolution results in considerably
higher projected melt for HIRHAM, mainly driven by the melt–albedo feedback. As shown in Fig. 7, HIRHAM stands out
throughout the simulation. The projected melt anomalies over the ice shelves reach $+903 \pm 90 \text{ Gt yr}^{-1}$ for HIRHAM, com-
pared to $+584 \pm 84 \text{ Gt yr}^{-1}$ for MAR, $+413 \pm 57 \text{ Gt yr}^{-1}$ for RACMO, and $+675 \pm 86 \text{ Gt yr}^{-1}$ for CESM (Table 3). As a
350 result of the high refreezing rates simulated by HIRHAM over the ice shelves, the firn progressively loses retention and cold
capacity (Fig. 7d). The curve shows an inflection point around 259–260 K, indicating the temperature at which the firn reaches
its maximum refreezing capacity. Beyond this threshold, successive melt–refreeze cycles further reduce firn porosity, limiting
water storage and refreezing, increasing the fraction of meltwater that is evacuated as runoff (Fig. 7h). Over the grounded ice,
HIRHAM also produces higher melt and refreezing rates from the start of the simulation (by factors of 6 and 4.5 relative to
355 MAR and RACMO, Table S1). This results in a strong melt trend; however, the firn’s maximum refreezing capacity has not
yet been reached. The resulting runoff over the grounded ice is nevertheless significantly higher compared to the other models,
but it remains small relative to the local precipitation, as illustrated in Fig. 4. However, this SWN runaway behaviour and the
high melt and refreezing rates at the start of the simulation cannot be explained by differences in the baseline surface energy
balance, surface albedo or downwelling longwave radiation (Fig. S3). Nevertheless, despite relative agreement on the contem-
porary SMB, these findings raise serious questions about the plausibility of HIRHAM’s simulated melt and refreezing rates
360 under current climate conditions.

MAR and RACMO are closely aligned in both their melt and refreezing rates over the reference period (Table S1) and in their
365 evolution with temperature (Fig. 7). Because melt rates are comparable at a given temperature, the near surface temperature
offset leads MAR to reach stronger melt than RACMO at the end of the simulation, with projected temperatures of 263.2 ± 0.5
K and 261.9 ± 0.4 K, respectively, corresponding to differences of 171 Gt yr^{-1} over the ice shelves and 150 Gt yr^{-1} over
the grounded ice. Refreezing in the two models evolves in parallel, but is shifted in temperature (2 °C over grounded ice and
1.3 °C over the shelves). This shift translates into differences in refreezing for the same melt rate and therefore contribute to
370 the divergence in runoff between MAR and RACMO (Fig. 7h). This divergence is further amplified by structural differences
in the firn representation: the higher retention capacity prescribed in MAR (5% versus 2% in RACMO) partly compensates for
its thinner firn, while the initially warmer MAR snowpack likely limits refreezing efficiency regardless of firn air content. In
addition, lower snowfall accumulation over the ice shelves in MAR reduces firn renewal, and enhanced rainfall associated with
warmer conditions further promotes runoff.

For CESM, the projected melt evolution over the ice shelves closely follows that of MAR and RACMO. Its similarity to
375 MAR in terms of near surface temperature (Fig. 5) translates into comparable future melt anomalies, with a difference of only
 91 Gt yr^{-1} , which is on the same order as their interannual variability 84 Gt yr^{-1} for MAR and 86 Gt yr^{-1} for CESM. Over
the grounded ice, CESM projects a stronger melt increase, akin to HIRHAM. However, CESM predicts persistent and substan-
tial refreezing that continues to grow without reaching a plateau, thereby limiting the acceleration of runoff. In addition, CESM
exhibits an integrated runoff component evolution over the entire ice shelves that is remarkably similar to MAR and RACMO,



380 despite its native resolution of 110 km.

Although liquid precipitation represents only a small fraction of the total liquid water (melt + rainfall) at the surface, accounting for 8% in HIRHAM, 10% in MAR, 7% in RACMO, and 17% in CESM in future anomalies (Table 3), the models exhibit divergent rainfall rates for similar near-surface temperatures, with HIRHAM and CESM producing substantially higher
385 rates than MAR and RACMO for a given temperature (Fig. 7). However, HIRHAM shows an evolution comparable to MAR, reaching similar mean (2080-2099) liquid precipitation rates of $78 \pm 15 \text{ Gt yr}^{-1}$ and $66 \pm 12 \text{ Gt yr}^{-1}$ over the ice shelves, and $83 \pm 17 \text{ Gt yr}^{-1}$ and $77 \pm 16 \text{ Gt yr}^{-1}$ over grounded ice, respectively. This indicates that liquid precipitation does not contribute to the runoff divergence between HIRHAM and MAR. As for MAR and RACMO, they again display a very similar rainfall–temperature relationship (Fig. 7e, f). Nevertheless, the temperature offset between MAR and RACMO results in
390 higher rainfall rates in MAR by the end of the simulation compared to RACMO ($27 \pm 7 \text{ Gt yr}^{-1}$ over grounded ice and $33 \pm 7 \text{ Gt yr}^{-1}$ over the ice shelves), contributing to their runoff differences. The high liquid precipitation rates reached by CESM ($171 \pm 20 \text{ Gt yr}^{-1}$ and $160 \pm 17 \text{ Gt yr}^{-1}$) explain its similarity in runoff compared to MAR, despite much greater refreezing rates in CESM (Fig. 7c, d) and very similar melt rates (Fig. 7a, b). This high estimated liquid precipitation in CESM has already been reported by McIlhattan et al. (2020), who identified a systematic rainfall bias in the model. While rainfall remains
395 a relatively small contributor overall compared to surface meltwater production (Donat-Magnin et al., 2020), it nonetheless affects the surface hydrological regime and hence runoff by adding liquid water to the surface.

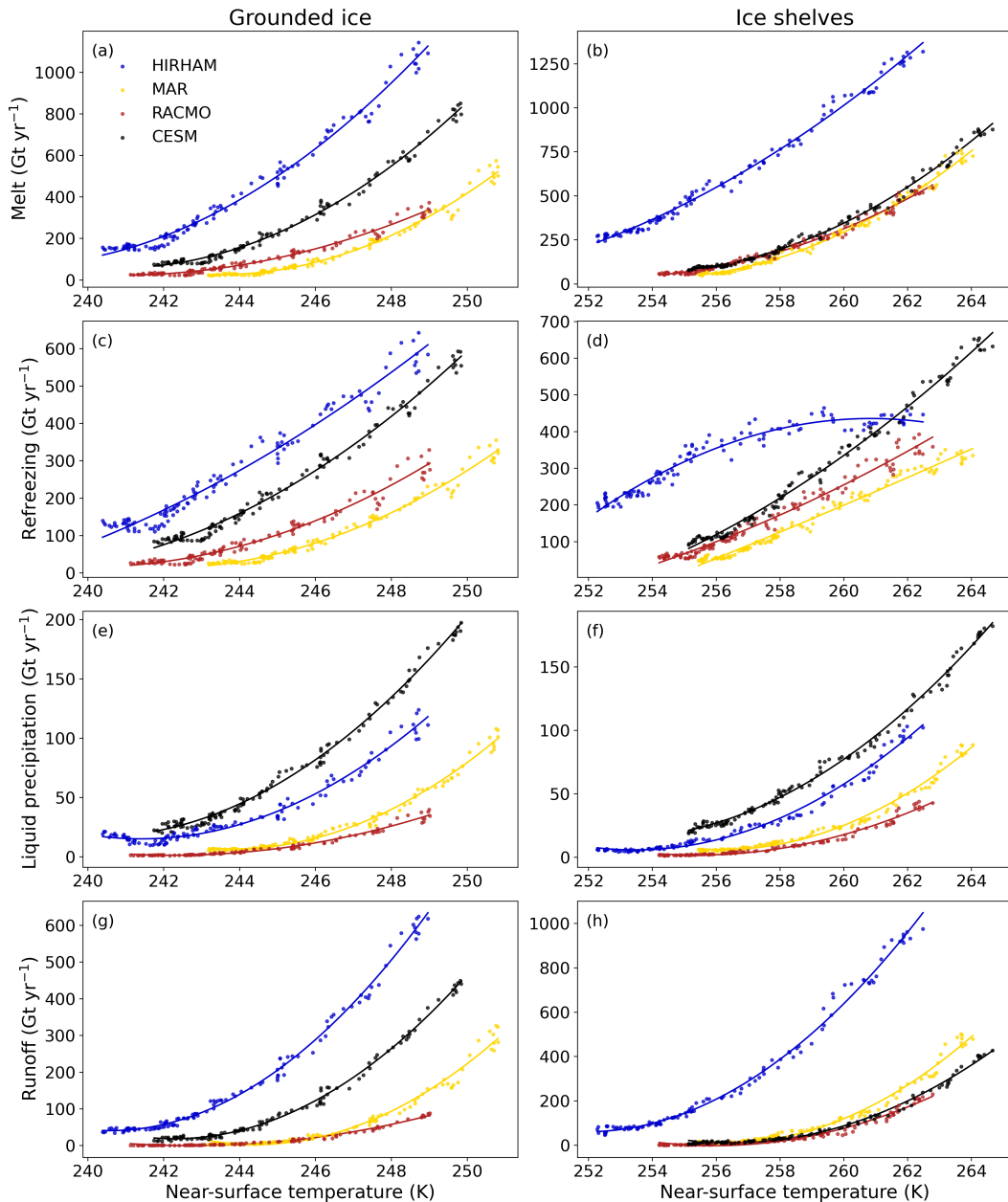


Figure 7. Absolute melt (a, b), refreezing (c, d), liquid precipitation (e, f) and runoff (g, h) in Gt yr^{-1} , as function of the absolute annual near-surface air temperature in K. For the models MAR (yellow), HIRHAM (blue), and RACMO (red) driven by CESM (black) under the SSP5-8.5 scenario. Values are integrated over grounded (left) and floating (right) parts of the ice sheet. Note that the Y-axis scales differ between grounded and floating ice due to the difference in surface areas. A 5-year running mean is applied for clarity.



This surface hydrological regime can be described by the ratio of surface liquid water (melt plus rainfall) to net accumulation (snowfall minus sublimation), defined in the literature as the Melt Over Accumulation (MOA) ratio (Pfeffer et al., 1991; Donat-Magnin et al., 2020; Van Wessem et al., 2023). Theoretical considerations suggest that, when MOA exceeds 0.7, that
400 is, when liquid water input at the surface reaches 70% of net accumulation, the snowpack can no longer retain and renew pore space, triggering runoff and/or melt-pond formation, thereby increasing the risk of ice-shelf disintegration via hydrofracturing.

Figure 8 shows the integrated surface liquid water and net accumulation over grounded ice (left panel) and ice shelves (right panel). Two distinct regimes emerge over ice shelves: HIRHAM undergoes a much earlier transition than the other models.
405 While its simulated accumulation remains comparable to the other RCMs, excess rainfall and melt push HIRHAM beyond the threshold as early as 252.5 ± 0.4 K, several degrees earlier than MAR, RACMO, and CESM (258.9 ± 0.5 K, 260.0 ± 0.6 K, and 258.4 ± 0.2 K, respectively) represented by the vertical dotted lines in Fig. 8. This is particularly striking, as HIRHAM's mean temperature during the reference period (1995–2014), is 253.2 ± 0.7 K. This suggests an unrealistically early onset of runaway runoff in HIRHAM, unlike in the other models, where melt and accumulation remain more balanced, making such
410 a scenario far less likely. We also note that over ice shelves, MAR simulates lower accumulation than RACMO (by about 86 Gt yr^{-1}). For comparable melt rates, this reduced accumulation causes MAR to reach the threshold at lower temperatures than RACMO, thereby promoting runoff. In contrast, this threshold is not reached over the integrated grounded ice, despite the large accumulation.

415 The spatial distribution of the temperature anomalies at which the MOA threshold of 0.7 is reached further supports this interpretation (Fig. 9). HIRHAM stands out by reaching the threshold at near-zero or even negative temperature anomalies, indicating that this critical state exposing ice shelves to a risk of destabilization already occurs during or even before the reference period across most ice shelves (Fig. S4). In contrast, MAR, RACMO, and CESM show broadly consistent threshold anomalies,
420 with only localized differences—particularly over the Filchner–Ronne and Ross shelves—likely reflecting spatial variations in accumulation and melt intensity among the models. Despite these local discrepancies, a coherent pattern emerges over key regions such as the Amery and Larsen ice shelves, where the threshold corresponds closely to the mean temperature of the reference period. This agreement is consistent with observations from the Amery Ice Shelf which experiences intense surface meltwater ponding (Spergel et al., 2021), as well as the Larsen sector where successive collapses of ice shelves—interpreted as being linked to enhanced surface melt—were documented between 1995 and 2020 (e.g., Rack and Rott, 2004; Scambos et al.,
425 2009; Willie et al., 2022; Scambos et al., 2004).

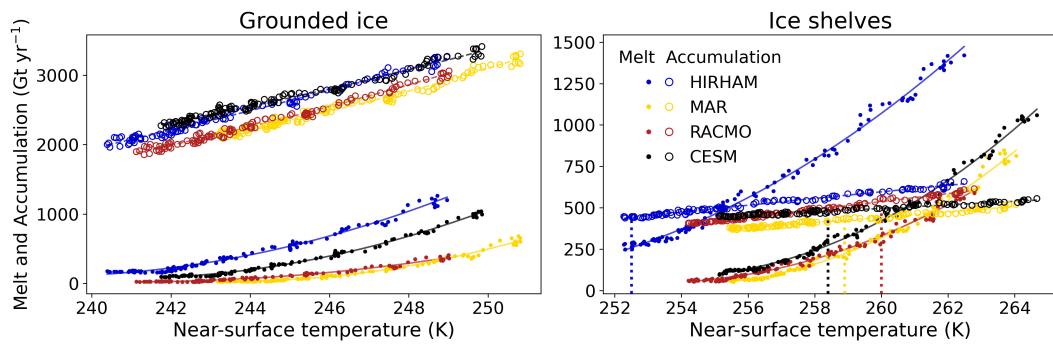


Figure 8. Absolute values of liquid water (melt + rainfall, filled dots) and accumulation (snowfall - sublimation, open circles), expressed in Gt yr^{-1} , as a function of the absolute annual near-surface air temperature in K. For the models MAR (yellow), HIRHAM (blue), and RACMO (red) driven by CESM (black) under the SSP5-8.5 scenario. The respective vertical dotted lines indicate the temperature at MOA=0.7. Values are integrated over grounded (left) and floating (right) parts of the ice sheet. Note that the Y-axis scales differ between grounded and floating ice due to the difference in surface areas. A 5-year running mean is applied for clarity.

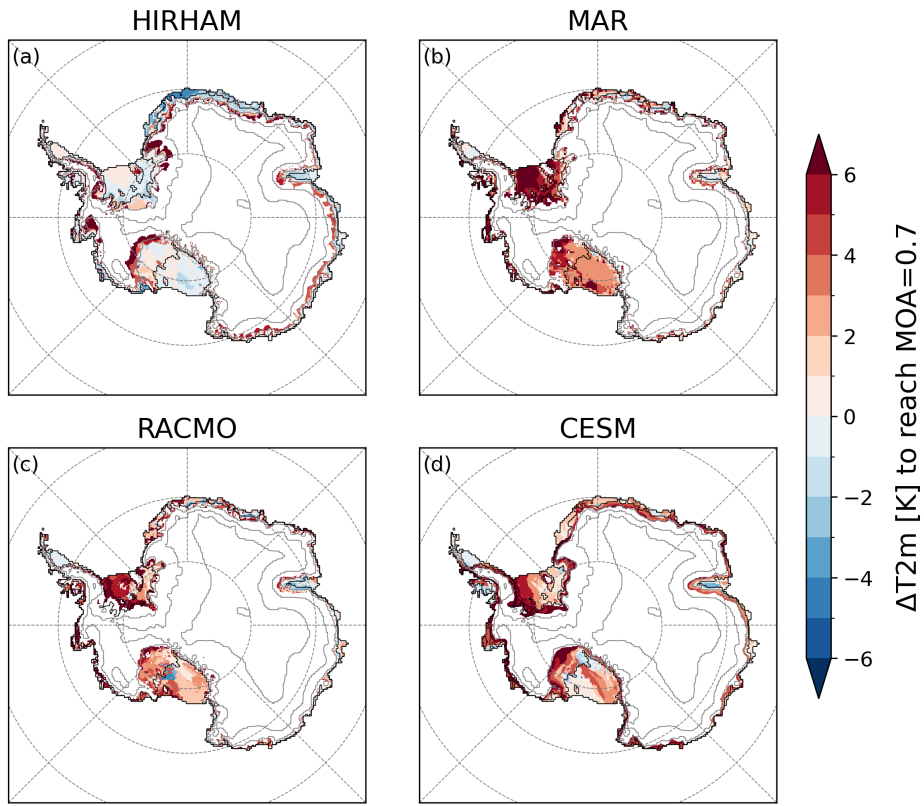


Figure 9. Near-surface temperature anomaly in K, at each grid point when the Melt-over-Accumulation ratio reaches the threshold of 0.7 (MOA = 0.7). For HIRHAM (a), MAR (b), RACMO (c), and CESM (d) under the SSP5-8.5 scenario. MOA values are calculated using a 5-year running mean.

4 Summary and conclusion

In this study, we investigated the causes of inter-model variability in projections of the Antarctic SMB until the end of the 21st century through a comparative analysis of three RCMs—MAR, RACMO, and HIRHAM—and their common driving ESM, CESM under the high-emission SSP5-8.5 scenario. In addition to ESMs, RCMs, thanks to their finer resolution and 430 detailed physics specifically adapted to polar regions, are considered useful complementary tools for producing SMB projections and providing atmospheric forcings to ice sheet models. The inter-model variability revealed here emphasizes the need for continued evaluation and intercomparison of regional models to better constrain uncertainties in SMB projections. Despite 435 identical boundary conditions, the projected SMB strongly diverges over the ice shelves: HIRHAM simulates a strong decline of $-529 \pm 72 \text{ Gt yr}^{-1}$, MAR a more moderate loss of $-209 \pm 58 \text{ Gt yr}^{-1}$, while RACMO maintains a near-equilibrium SMB of $+25 \pm 19 \text{ Gt yr}^{-1}$. These differences mainly stem from the spread in meltwater runoff anomalies: $+775 \pm 94 \text{ Gt yr}^{-1}$ for HIRHAM, $+390 \pm 76 \text{ Gt yr}^{-1}$ for MAR and $+170 \pm 37 \text{ Gt yr}^{-1}$ for RACMO. CESM also departs from the three RCMs,



projecting a SMB decrease of $-118 \pm 36 \text{ Gt yr}^{-1}$ driven by a runoff increase of $+329 \pm 59 \text{ Gt yr}^{-1}$ (Table 4). In contrast, over the grounded ice sheet, inter-model variability remains limited, with similar SMB anomalies ($+610 \pm 69 \text{ Gt yr}^{-1}$ for HIRHAM, $+757 \pm 85 \text{ Gt yr}^{-1}$ for MAR, $+870 \pm 93 \text{ Gt yr}^{-1}$ for RACMO, and $+657 \pm 80 \text{ Gt yr}^{-1}$ for CESM), mainly 440 driven by increased snowfall while runoff remains relatively less significant.

A key source of uncertainty lies in the representation of present-day melt rates: within our ensemble, HIRHAM simulates melt and refreezing rates several times higher than MAR and RACMO, which shows closer agreement under current conditions (Fig. 2, Table 3 and Fig. 7a, b). This overestimation is further illustrated in Sec. 3.1.2, where HIRHAM produces 3.5 times more 445 Cumulative Melting Surface than SSM/I observation (Fig. 2, Table 3). The present-day melt rate governs the nonlinear temperature–melt relationship, and thus the magnitude of future runoff and SMB anomalies. The potential melt bias in HIRHAM during the reference period, and its contemporary melt rates comparable to those projected by MAR and RACMO at the end of the century, certainly accounts for this model divergence which is particularly pronounced under the high-emission scenario 450 SSP5-8.5, amplifying the uncertainty surrounding the extent of projected changes. Although the divergence in HIRHAM melt rates is most striking over ice shelves, the same tendency toward excessive melt or an overly strong temperature sensitivity is also present over grounded ice, where it is partly masked by a larger concurrent increase in snowfall that still dominates 455 SMB changes. The combination of high surface liquid water production and elevated refreezing rates already during the contemporary period, both contributing to enhance the melt–albedo feedback and limit additional firn retention capacity, accounts for the much stronger intensification of runoff in HIRHAM over the ice shelves compared with the other models. As a result, 460 HIRHAM crosses the MOA threshold for meltwater ponding much earlier, amplifying runoff and increasing the vulnerability of ice shelves to hydrofracture-induced destabilization. Notably, most ice shelves in HIRHAM already exceed this threshold 465 during the reference period (Fig. 9).

For MAR and RACMO, although they simulate similar melt and runoff rates under present-day conditions, their projections 460 diverge by the end of the century: runoff anomalies over the shelves reach $+390 \pm 76 \text{ Gt yr}^{-1}$ in MAR compared to $+170 \pm 37 \text{ Gt yr}^{-1}$ in RACMO (Table 4). This divergence arises from two factors: (1) difference in surface liquid water production, when 465 toward the end of the simulation MAR produces more liquid water than RACMO owing to systematically higher near-surface temperature ; and (2) differences in refreezing rates when, for a given temperature, MAR refreezes less than RACMO. In addition, lower accumulation over the ice shelves in MAR reduces firn renewal, further promoting runoff. Despite these differences, 470 the two models remain broadly consistent in their overall behavior. In CESM, refreezing remains substantial, yet the increased occurrence of surface liquid water is not sufficiently balanced, leading to a projected runoff increase of $+329 \pm 59 \text{ Gt yr}^{-1}$ over the shelves—comparable in magnitude to MAR.

Remarkably, CESM, despite its coarse resolution and its design as an Earth System Model rather than a polar-oriented one, 470 performs comparably to the regional models. This reflects the substantial efforts made to improve the representation of ice-sheet surfaces in CESM/CLM, which have helped narrow the gap between global and regional models in simulating ice-sheet



surface mass balance.

The melt rates produced by HIRHAM at the beginning of the simulation cannot be fully explained with the available model
475 outputs. There is no direct link between high surface energy fluxes and the simulated melt rates, nor can the melt trends be attributed to low albedo values at the beginning of the simulation (Fig. S3). Differences in how HIRHAM translates large-scale warming into local surface conditions were ruled out as a potential explanation, since its projected 500 hPa temperature closely matches that of the other models (Fig. S5). This suggests that other factors inherent to the model physics may contribute, including the model-specific melt–albedo feedback, treatment of water and the absence of feedback with atmosphere
480 (e.g. cooling of the near-surface air during surface melt due to the consumption of latent heat, or conversely, enhanced warming of the near-surface air through sensible heat transfer when surface temperatures increase following albedo reduction after melt).

Other factors likely contribute to the divergences observed in regional projections, particularly in the representation of firn structure and the parameterizations governing meltwater production, retention, refreezing, and runoff. Although a thinner firn
485 column (such as the 20 m used in MAR compared with at least 30 m in RACMO) would normally reduce pore volume and retention potential, this effect can be largely offset by differences in prescribed maximum water retention capacity (5% in MAR versus 2% in RACMO). Contrasts in meltwater percolation schemes further influence how firn air content evolves under sustained melt: HIRHAM employs a Darcy-flow formulation, whereas the other models use simplified bucket-scheme approaches, leading to different rates of change in firn retention capacity and pore-space depletion. Under dry conditions, differences in
490 firn densification schemes determine how quickly firn air content decreases, while differences in prescribed density of newly deposited snow affects how effectively fresh snowfall can renew firn air content. The conditions under which runoff initiates also vary across models, adding another source of divergence. In CESM, and RACMO, the entire firn layer must reach its irreducible water content before runoff occurs, whereas HIRHAM and MAR permit fractional runoff when percolating water encounters ice lenses or impermeable ice layers. Albedo parameterizations further modulate the melt response to warming.
495 HIRHAM prescribes albedo as a function of surface temperature, whereas the other models incorporate the evolution of snow grain size and/or density, resulting in differing expressions of the melt–albedo feedback. Finally, a potentially significant limitation of the current models lies in their simplified representation, or complete non-consideration, of meltwater ponding on the ice surface. The formation of surface meltwater ponding can substantially reduce the local albedo, leading to enhanced solar absorption and further accelerating melt rates (e.g. Dell et al., 2024), while at the same time, a portion of the ponded water can
500 refreeze, partly offsetting mass loss that would otherwise result from runoff (Goutard et al., 2025).

Finally, we would like to note that after 30 years of service the HIRHAM5 model was retired shortly after these simulations were complete, to be replaced by the HARMONIE-Climate system model (e.g. Verro et al., 2025). These will therefore be the last results published from HIRHAM, but the analysis here shows how important continuous assessment, improvement,
505 development and evaluation of regional climate models is.



510 A promising way to reduce these structural and parametric uncertainties would be to produce projections initialized with a common firn state, using for instance identical vertical discretization and shared parameterizations, to better isolate differences arising from the models' physical evolution. However, progress is currently limited by the restricted set of available model outputs. More advanced diagnostics of firn evolution and melt-albedo feedbacks would require, at minimum, vertically resolved firn properties (depth/thickness, temperature, liquid water content, and density) down to the close-off density. Providing these outputs in future intercomparison exercises would greatly strengthen model evaluation and help clarify the processes driving divergence among models.

515 These results highlight the need to continue the development and evaluation of climate models, particularly regarding the key physical processes governing SMB and involving surface hydrology (The Firn Symposium team: Amory et al., 2024), in order to better constrain uncertainties in estimates of Antarctic ice-sheet contribution to sea-level rise.

Data availability. Python scripts developed for this study as well as all required data are available at (draft zenodo version) <https://zenodo.org/record/XXXXXXX>.

520 *Author contributions.* CA and BH designed the study. Model simulations were performed by CA (MAR), XX (RACMO), FB, MO, NH, RM (HIRHAM), and RW (CESM2). RRW provided expertise in the analysis of CESM2 outputs. CA performed the regridding of the model outputs with support from HG. BE conducted the main analysis and wrote the first draft of the manuscript, with contributions from CA. All authors contributed to the interpretation of the results and to the writing of the manuscript.

Competing interests. At least one of the co-authors is a member of the editorial board of The Cryosphere

525 *Acknowledgements.* This work was supported by the European Union's Horizon 2020 Research and Innovation Programme under grant agreement No. 869304 (PROTECT), and by the Agence Nationale de la Recherche - France 2030 as part of the PEPR TRACCS programme under grant numbers ANR-22-EXTR-0008 (IMPRESSION-ESM) and ANR-22-EXTR-0010 (ISCLIM). Computational resources for MAR runs have been provided by the Consortium des Équipements de Calcul Intensif (CÉCI), funded by the F.R.S.-FNRS under grant no. 2.5020.11. FB, MO, NH and RM are supported by the Danish State through the National Centre for Climate Research (NCKF); furthermore, 530 NH has been supported by the Novo Nordisk Foundation project PRECISE (grant no. 310 NNF23OC0081251). Resources were provided by Sigma2 - the National Infrastructure for High Performance Computing and Data Storage in Norway through projects, NN11016K, NN8085K, NN5011K, NS11016K, NS8085K and NS5011K. WJvdB is supported by PolarRES (grant no. 101003590), a project of the European Union's Horizon 2020 research and innovation programme.



References

535 Agosta, C., Amory, C., Kittel, C., Orsi, A., Favier, V., Gallée, H., Van Den Broeke, M. R., Lenaerts, J., Van Wessem, J. M., Van De Berg, W. J., et al.: Estimation of the Antarctic surface mass balance using the regional climate model MAR (1979–2015) and identification of dominant processes, *The Cryosphere*, 13, 281–296, <https://doi.org/10.5194/tc-13-281-2019>, 2019.

Agosta, C., Kittel, C., Amory, C., Edwards, T., and Davrinche, C.: Evaluation of CMIP5 and CMIP6 global climate models in the Arctic and Antarctic regions, atmosphere and surface ocean, *Tech. Rep.*, EGU22-11363, <https://doi.org/10.5194/egusphere-egu22-11363>, 2022.

540 Bamber, J., Gomez-Dans, J., and Griggs, J.: A new 1 km digital elevation model of the Antarctic derived from combined satellite radar and laser data—Part 1: Data and methods, *The Cryosphere*, 3, 101–111, <https://doi.org/10.5194/tc-3-101-2009>, 2009.

Boberg, F., Mottram, R., Hansen, N., and Simonsen, S.: The Challenge of Present Day and Future Climate in Antarctica: An Intercomparison of Regional Climate Models., in: *Geophysical Research Abstracts*, vol. 21, ISSN 1029-7006, 2019.

Boberg, F., Mottram, R., Hansen, N., Yang, S., and Langen, P. L.: Uncertainties in projected surface mass balance over the polar ice sheets from dynamically downscaled EC-Earth models, *The Cryosphere*, 16, 17–33, <https://doi.org/10.5194/tc-16-17-2022>, 2022.

545 Christensen, O. B., Drews, M., Christensen, J. H., Dethloff, K., Ketelsen, K., Hebestadt, I., and Rinke, A.: The HIRHAM Regional Climate Model, Version 5 (beta), *Tech. Rep. Technical Report 06-17*, Danish Meteorological Institute, Copenhagen, Denmark, <http://www.dmi.dk/dmi/tr06-17>, 2007.

Clem, K. R., Adusumilli, S., Baiman, R., Banwell, A. F., Barreira, S., Beadling, R. L., Bozkurt, D., Colwell, S., Coy, L., Datta, R. T., De Laat, J., du Plessis, M., Dunmire, D., Fogt, R. L., Freeman, N. M., Fricker, H. A., Gardner, A. S., Johnson, B., Keller, L. M., Lazzara, M. A., Lieser, J. L., MacFerrin, M., MacGilchrist, G. A., MacLennan, M. L., Massom, R. A., Mazloff, M. R., Mote, T. L., Nash, E. R., Newman, P. A., Norton, T., Petropavlovskikh, I., Pitts, M., Reid, P., Santee, M. L., Scambos, T. A., Schulz, C., Shi, J.-R., Souza, E., Stammerjohn, S., Strahan, S. E., Thompson, A. F., Wille, J. D., Wilson, E., and Veasey, S. W.: Antarctica and the Southern Ocean, *Bulletin of the American Meteorological Society*, 104, S322–S365, <https://doi.org/10.1175/BAMS-D-23-0077.1>, 2023.

550 555 Cook, A. J., Murray, T., Luckman, A., Vaughan, D. G., and Barrand, N. E.: A new 100-m Digital Elevation Model of the Antarctic Peninsula derived from ASTER Global DEM: methods and accuracy assessment, *Earth system science data*, 4, 129–142, <https://doi.org/10.5194/essd-4-129-2012>, 2012.

Coulon, V., Klose, A. K., Kittel, C., Edwards, T., Turner, F., Winkelmann, R., and Pattyn, F.: Disentangling the drivers of future Antarctic ice loss with a historically-calibrated ice-sheet model, <https://doi.org/10.5194/egusphere-2023-1532>, eGUsphere preprint, 2023.

560 Danabasoglu, G., Lamarque, J.-F., Bacmeister, J., Bailey, D., DuVivier, A., Edwards, J., Emmons, L., Fasullo, J., Garcia, R., Gettelman, A., et al.: The community earth system model version 2 (CESM2), *Journal of Advances in Modeling Earth Systems*, 12, e2019MS001916, <https://doi.org/10.1029/2019MS001916>, 2020.

Delhasse, A., Beckmann, J., Kittel, C., and Fettweis, X.: Coupling MAR (Modèle Atmosphérique Régional) with PISM (Parallel Ice Sheet Model) mitigates the positive melt–elevation feedback, *The Cryosphere*, 18, 633–651, <https://doi.org/10.5194/tc-18-633-2024>, 2024.

565 Dell, R. L., Willis, I. C., Arnold, N. S., Banwell, A. F., and de Roda Husman, S.: Substantial contribution of slush to meltwater area across Antarctic ice shelves, *Nature Geoscience*, 17, 624–630, <https://doi.org/10.1038/s41561-024-01466-6>, 2024.

Donat-Magnin, M., Jourdain, N. C., Gallée, H., Amory, C., Kittel, C., Fettweis, X., Wille, J. D., Favier, V., Drira, A., and Agosta, C.: Interannual variability of summer surface mass balance and surface melting in the Amundsen sector, West Antarctica, *The Cryosphere*, 14, 229–249, <https://doi.org/10.5194/tc-14-229-2020>, 2020.



570 Dunmire, D., Lenaerts, J. T., Datta, R. T., and Gorte, T.: Antarctic surface climate and surface mass balance in the Community Earth System Model version 2 during the satellite era and into the future (1979–2100), *The Cryosphere*, 16, 4163–4184, <https://doi.org/10.5194/tc-16-4163-2022>, 2022.

575 Edwards, T. L., Nowicki, S., Marzeion, B., Hock, R., Goelzer, H., Seroussi, H., Jourdain, N. C., Slater, D. A., Turner, F. E., Smith, C. J., McKenna, C. M., Simon, E., Abe-Ouchi, A., Gregory, J. M., Larour, E., Lipscomb, W. H., Payne, A. J., Shepherd, A., Agosta, C., Alexander, P., Albrecht, T., Anderson, B., Asay-Davis, X., Aschwanden, A., Barthel, A., Bliss, A., Calov, R., Chambers, C., Champollion, N., Choi, Y., Cullather, R., Cuzzone, J., Dumas, C., Felikson, D., Fettweis, X., Fujita, K., Galton-Fenzi, B. K., Gladstone, R., Golledge, N. R., Greve, R., Hattermann, T., Hoffman, M. J., Humbert, A., Huss, M., Huybrechts, P., Immerzeel, W., Kleiner, T., Kraaijenbrink, P., Le Clec'h, S., Lee, V., Leguy, G. R., Little, C. M., Lowry, D. P., Malles, J.-H., Martin, D. F., Maussion, F., Morlighem, M., O'Neill, J. F., Nias, I., Pattyn, F., Pelle, T., Price, S. F., Quiquet, A., Radić, V., Reese, R., Rounce, D. R., Rückamp, M., Sakai, A., Shafer, C., Schlegel, N.-J., Shannon, S., Smith, R. S., Straneo, F., Sun, S., Tarasov, L., Trusel, L. D., Van Breedam, J., van de Wal, R., van den Broeke, M., Winkelmann, R., Zekollari, H., Zhao, C., Zhang, T., and Zwinger, T.: Projected land ice contributions to twenty-first-century sea level rise, *Nature*, 593, 74–82, <https://doi.org/10.1038/s41586-021-03302-y>, 2021.

580 Eerola, K.: About the performance of HIRLAM version 7.0, *Hirlam Newsletter*, 51, 93–102, https://hirlam.org/index.php/hirlam-documentation/doc_view/473-hirlam-newsletter-no-51-article14-eerola-performance-hirlam7-0, 2006.

585 Eyring, V., Bony, S., Meehl, G. A., Senior, C. A., Stevens, B., Stouffer, R. J., and Taylor, K. E.: Overview of the Coupled Model Intercomparison Project Phase 6 (CMIP6) experimental design and organization, *Geoscientific Model Development*, 9, 1937–1958, <https://doi.org/10.5194/gmd-9-1937-2016>, 2016.

590 Fettweis, X., Box, J. E., Agosta, C., Amory, C., Kittel, C., Lang, C., Van As, D., Machguth, H., and Gallée, H.: Reconstructions of the 1900–2015 Greenland ice sheet surface mass balance using the regional climate MAR model, *The Cryosphere*, 11, 1015–1033, <https://doi.org/10.5194/tc-11-1015-2017>, 2017.

595 Fettweis, X., Hofer, S., Krebs-Kanzow, U., Amory, C., Aoki, T., Berends, C. J., Born, A., Box, J. E., Delhasse, A., Fujita, K., et al.: GrSMB-MIP: intercomparison of the modelled 1980–2012 surface mass balance over the Greenland Ice Sheet, *The Cryosphere*, 14, 3935–3958, <https://doi.org/10.5194/tc-14-3935-2020>, 2020.

Flanner, M. G. and Zender, C. S.: Snowpack radiative heating: Influence on Tibetan Plateau climate, *Geophysical Research Letters*, 32, L06 501, <https://doi.org/10.1029/2004GL022076>, 2005.

595 Flanner, M. G., Zender, C. S., Randerson, J. T., and Rasch, P. J.: Present-day climate forcing and response from black carbon in snow, *Journal of Geophysical Research*, 112, D11 202, <https://doi.org/10.1029/2006JD008003>, 2007.

600 Fox-Kemper, B., Hewitt, H., Xiao, C., Aðalgeirsdóttir, G., Drijfhout, S., Edwards, T., Golledge, N., Hemer, M., Kopp, R., Krinner, G., Mix, A., Notz, D., Nowicki, S., Nurhati, I., Ruiz, L., Sallée, J.-B., Slangen, A., and Yu, Y.: Ocean, Cryosphere and Sea Level Change, in: *Climate Change 2021: The Physical Science Basis. Contribution of Working Group I to the Sixth Assessment Report of the Intergovernmental Panel on Climate Change*, edited by Masson-Delmotte, V., Zhai, P., Pirani, A., Connors, S., Péan, C., Berger, S., Caud, N., Chen, Y., Goldfarb, L., Gomis, M., Huang, M., Leitzell, K., Lonnoy, E., Matthews, J., Maycock, T., Waterfield, T., Yelekçi, O., Yu, R., and Zhou, B., pp. 1211–1362, Cambridge University Press, Cambridge, United Kingdom and New York, NY, USA, <https://doi.org/10.1017/9781009157896.011>, 2021.

605 Fretwell, P., Pritchard, H. D., Vaughan, D. G., Bamber, J. L., Barrand, N. E., Bell, R., Bianchi, C., Bingham, R., Blankenship, D. D., Casassa, G., et al.: Bedmap2: improved ice bed, surface and thickness datasets for Antarctica, *The cryosphere*, 7, 375–393, <https://doi.org/10.5194/tc-7-375-2013>, 2013.



Gadde, S. and van de Berg, W. J.: Contribution of blowing snow sublimation to the surface mass balance of Antarctica, <https://doi.org/10.5194/egusphere-2024-116>, eGUsphere preprint, 2024.

610 Gallée, H.: Simulation of the mesocyclonic activity in the Ross Sea, Antarctica, *Monthly Weather Review*, 123, 2051–2069, [https://doi.org/10.1175/1520-0493\(1995\)123<2051:SOTMAI>2.0.CO;2](https://doi.org/10.1175/1520-0493(1995)123<2051:SOTMAI>2.0.CO;2), 1995.

Gallée, H. and Schayes, G.: Development of a three-dimensional meso- γ primitive equation model: katabatic winds simulation in the area of Terra Nova Bay, Antarctica, *Monthly Weather Review*, 122, 671–685, [https://doi.org/10.1175/1520-0493\(1994\)122<0671:DOATDM>2.0.CO;2](https://doi.org/10.1175/1520-0493(1994)122<0671:DOATDM>2.0.CO;2), 1994.

615 Gettelman, A.: The Whole Atmosphere Community Climate Model Version 6 (WACCM6): Model description and validation, *Journal of Geophysical Research: Atmospheres*, 124, 13 017–13 043, <https://doi.org/10.1029/2019JD030943>, 2019.

Glaude, Q., Noël, B., Olesen, M., Van den Broeke, M., van de Berg, W. J., Mottram, R., Hansen, N., Delhasse, A., Amory, C., Kittel, C., et al.: A factor two difference in 21st-century Greenland ice sheet surface mass balance projections from three regional climate models under a strong warming scenario (SSP5-8.5), *Geophysical Research Letters*, 51, e2024GL111902, <https://doi.org/10.1029/2024GL111902>, 2024.

620 Goutard, A., Réveillet, M., Brun, F., Six, D., Fourteau, K., Amory, C., Fettweis, X., Fructus, M., Khadka, A., and Lafaysse, M.: Explicit representation of liquid water retention over bare ice using the SURFEX/ISBA-Crocus model: implications for mass balance at Mera glacier (Nepal), <https://doi.org/10.5194/egusphere-2025-2947>, eGUsphere preprint (discussion started 14 Aug 2025), 2025.

Hansen, N., Langen, P. L., Boberg, F., Forsberg, R., Simonsen, S. B., Thejll, P., Vandecrux, B., and Mottram, R.: Downscaled surface mass balance in Antarctica: impacts of subsurface processes and large-scale atmospheric circulation, *The Cryosphere*, 15, 4315–4333, <https://doi.org/10.5194/tc-15-4315-2021>, 2021.

625 Hansen, N., Simonsen, S. B., Boberg, F., Kittel, C., Orr, A., Souverijns, N., van Wessem, J. M., and Mottram, R.: Impact of common ice mask in surface mass balance estimates over the Antarctic ice sheet, *The Cryosphere*, 16, 711–718, <https://doi.org/10.5194/tc-16-711-2022>, 2022.

Hansen, N., Orr, A., Zou, X., Boberg, F., Bracegirdle, T. J., Gilbert, E., Langen, P. L., Lazzara, M. A., Mottram, R., Phillips, T., Price, R., 630 Simonsen, S. B., and Webster, S.: The importance of cloud properties when assessing surface melting in an offline-coupled firn model over Ross Ice shelf, West Antarctica, *The Cryosphere*, 18, 2897–2916, <https://doi.org/10.5194/tc-18-2897-2024>, 2024.

Herrington, A. R., Lauritzen, P. H., Reed, K. A., Goldhaber, S., Eaton, B. E., and Gettelman, A.: Impact of grids and dynamical cores in CESM2.2 on the surface mass balance of the Greenland Ice Sheet, *Journal of Advances in Modeling Earth Systems*, 14, e2022MS003192, <https://doi.org/10.1029/2022MS003192>, 2022.

635 Hofsteenge, M. G., van de Berg, W. J., van Dalum, C., Verro, K., van Tiggelen, M., and van den Broeke, M.: On the non-linear response of Antarctic ice shelf surface melt to warming, *EGUsphere*, <https://doi.org/10.5194/egusphere-2025-4176>, preprint, 2025.

Hunke, E. C. and Lipscomb, W. H.: CICE: The Los Alamos Sea Ice Model: Documentation and Software User's Manual, Tech. Rep. LA-CC-06-012, Los Alamos National Laboratory, Los Alamos, New Mexico, USA, 2010.

Jakobs, C., Reijmer, C., Van den Broeke, M., Van de Berg, W., and Van Wessem, J.: Spatial variability of the snowmelt-albedo feedback in 640 Antarctica, *Journal of Geophysical Research: Earth Surface*, 126, e2020JF005696, <https://doi.org/10.1029/2020JF005696>, 2021a.

Jakobs, C. L., Reijmer, C. H., van den Broeke, M. R., van de Berg, W. J., and van Wessem, J. M.: Spatial Variability of the Snowmelt–Albedo Feedback in Antarctica, *Journal of Geophysical Research: Earth Surface*, 126, e2020JF005696, <https://doi.org/10.1029/2020JF005696>, 2021b.

Jourdain, N. C., Amory, C., Kittel, C., and Durand, G.: Changes in Antarctic surface conditions and potential for ice shelf hydrofracturing 645 from 1850 to 2200, *The Cryosphere*, 19, 1641–1674, <https://doi.org/10.5194/tc-19-1641-2025>, 2025.



Kittel, C., Amory, C., Agosta, C., Jourdain, N. C., Hofer, S., Delhasse, A., Doutreloup, S., Huot, P.-V., Lang, C., Fichefet, T., et al.: Diverging future surface mass balance between the Antarctic ice shelves and grounded ice sheet, *The Cryosphere*, 15, 1215–1236, <https://doi.org/10.5194/tc-15-1215-2021>, 2021.

Kittel, C., Amory, C., Hofer, S., Agosta, C., Jourdain, N. C., Gilbert, E., Le Toumelin, L., Vignon, É., Gallée, H., and Fettweis, X.: Clouds 650 drive differences in future surface melt over the Antarctic ice shelves, *The Cryosphere*, 16, 2655–2669, <https://doi.org/10.5194/tc-16-2655-2022>, 2022.

Kuipers Munneke, P., Picard, G., van den Broeke, M. R., Lenaerts, J. T. M., and van Meijgaard, E.: Insignificant change in Antarctic snowmelt 655 volume since 1979, *Geophysical Research Letters*, 39, L01501, <https://doi.org/10.1029/2011GL050207>, 2012.

Langen, P. L., Fausto, R. S., Vandecrux, B., Mottram, R. H., and Box, J. E.: Liquid water flow and retention on the Greenland 655 ice sheet in the regional climate model HIRHAM5: Local and large-scale impacts, *Frontiers in Earth Science*, 4, 110, <https://doi.org/10.3389/feart.2016.00110>, 2017.

Lawrence, D. M., Fisher, R. A., Koven, C. D., Oleson, K. W., Swenson, S. C., Bonan, G., Collier, N., Ghimire, B., Van Kampenhout, L., Kennedy, D., et al.: The Community Land Model version 5: Description of new features, benchmarking, and impact of forcing uncertainty, *Journal of Advances in Modeling Earth Systems*, 11, 4245–4287, <https://doi.org/10.1029/2018MS001583>, 2019.

Lenaerts, J. T., Medley, B., van den Broeke, M. R., and Wouters, B.: Observing and modeling ice sheet surface mass balance, *Reviews of 660 Geophysics*, 57, 376–420, <https://doi.org/10.1029/2018RG000622>, 2019.

Lenaerts, J. T. M. and van den Broeke, M. R.: Modeling drifting snow in Antarctica with a regional climate model: 2. Results, *Journal of Geophysical Research: Atmospheres*, 117, <https://doi.org/10.1029/2010JD015419>, 2012.

Li, L. and Pomeroy, J. W.: Estimates of Threshold Wind Speeds for Snow Transport Using Meteorological Data, *Journal of Applied Meteorology*, 36, 205–213, [https://doi.org/10.1175/1520-0450\(1997\)036<0205:EOTWSF>2.0.CO;2](https://doi.org/10.1175/1520-0450(1997)036<0205:EOTWSF>2.0.CO;2), 1997.

Ligtenberg, S., Helsen, M., and Van den Broeke, M.: An improved semi-empirical model for the densification of Antarctic firn, *The Cryosphere*, 5, 809–819, <https://doi.org/10.5194/tc-5-809-2011>, 2011.

Lucas-Picher, P., Wulff-Nielsen, M., Christensen, J. H., Aðalgeirsðóttir, G., Mottram, R., and Simonsen, S. B.: Very high resolution 670 regional climate model simulations over Greenland: Identifying added value, *Journal of Geophysical Research: Atmospheres*, 117, <https://doi.org/10.1029/2011JD016267>, 2012.

Machguth, H., Tedstone, A., Kuipers Munneke, P., Brils, M., Noël, B., Clerx, N., Jullien, N., Fettweis, X., and van den Broeke, M.: Runoff from Greenland's firn area – why do MODIS, RCMs and a firn model disagree?, *EGUsphere*, <https://doi.org/10.5194/egusphere-2024-2750>, preprint, 2024.

McIlhattan, E. A. et al.: Arctic Clouds and Precipitation in the Community Earth System Model Version 2, *Journal of Geophysical Research: 675 Atmospheres*, <https://doi.org/10.1029/2020JD032521>, 2020.

Mottram, R., Hansen, N., Kittel, C., Van Wessem, J. M., Agosta, C., Amory, C., Boberg, F., Van De Berg, W. J., Fettweis, X., Gossart, A., et al.: What is the surface mass balance of Antarctica? An intercomparison of regional climate model estimates, *The Cryosphere*, 15, 3751–3784, <https://doi.org/10.5194/tc-2019-333>, 2021.

Munneke, P. K., Van den Broeke, M., Lenaerts, J., Flanner, M., Gardner, A., and Van de Berg, W.: A new albedo parameterization 680 for use in climate models over the Antarctic ice sheet, *Journal of Geophysical Research. Atmospheres*, 116, 1CC, <https://doi.org/10.1029/2010JD015113>, 2011.

Nowicki, S., Goelzer, H., Seroussi, H., Payne, A. J., Lipscomb, W. H., Abe-Ouchi, A., Agosta, C., Alexander, P., Asay-Davis, X. S., Barthel, A., Bracegirdle, T. J., Cullather, R., Felikson, D., Fettweis, X., Gregory, J. M., Hattermann, T., Jourdain, N. C., Kuipers Munneke, P.,



685 Larour, E., Little, C. M., Morlighem, M., Nias, I., Shepherd, A., Simon, E., Slater, D., Smith, R. S., Straneo, F., Trusel, L. D., van den Broeke, M. R., and van de Wal, R.: Experimental protocol for sea level projections from ISMIP6 stand-alone ice sheet models, *The Cryosphere*, 14, 2331–2368, <https://doi.org/10.5194/tc-14-2331-2020>, 2020.

690 Noël, B., van de Berg, W. J., van Wessem, J. M., van Meijgaard, E., van As, D., Lenaerts, J. T. M., Lhermitte, S., Kuipers Munneke, P., Smeets, C. J. P. P., van Ulf, L. H., van de Wal, R. S. W., and van den Broeke, M. R.: Modelling the climate and surface mass balance of polar ice sheets using RACMO2 – Part 1: Greenland (1958–2016), *The Cryosphere*, 12, 811–831, <https://doi.org/10.5194/tc-12-811-2018>, 2018.

695 Otosaka, I. N., Shepherd, A., Ivins, E. R., Schlegel, N.-J., Amory, C., van den Broeke, M. R., Horwath, M., Joughin, I., King, M. D., Krinner, G., Nowicki, S., Payne, A. J., Rignot, E., Scambos, T., Simon, K. M., Smith, B. E., Sørensen, L. S., Velicogna, I., Whitehouse, P. L., A., G., Agosta, C., Ahlstrøm, A. P., Blazquez, A., Colgan, W., Engdahl, M. E., Fettweis, X., Forsberg, R., Gallée, H., Gardner, A., Gilbert, L., Gourmelen, N., Groh, A., Gunter, B. C., Harig, C., Helm, V., Khan, S. A., Kittel, C., Konrad, H., Langen, P. L., Lecavalier, B. S., Liang, C.-C., Loomis, B. D., McMillan, M., Melini, D., Mernild, S. H., Mottram, R., Mouginot, J., Nilsson, J., Noël, B., Pattle, M. E., Peltier, W. R., Pie, N., Roca, M., Sasgen, I., Save, H. V., Seo, K.-W., Scheuchl, B., Schrama, E. J. O., Schröder, L., Simonsen, S. B., Slater, T., Spada, G., Sutterley, T. C., Vishwakarma, B. D., van Wessem, J. M., Wiese, D., van der Wal, W., and Wouters, B.: Mass balance of the Greenland and Antarctic ice sheets from 1992 to 2020, *Earth System Science Data*, 15, 1597–1616, <https://doi.org/10.5194/essd-15-1597-2023>, 2023.

700 Pfeffer, W., Meier, M., and Illangasekare, T.: Retention of Greenland runoff by refreezing: Implications for projected future sea level change, *Journal of Geophysical Research: Oceans*, 96, 22 117–22 124, <https://doi.org/10.1029/91JC02502>, 1991.

705 Picard, G., Leduc-Leballeur, M., Banwell, A. F., Brucker, L., and Macelloni, G.: The sensitivity of satellite microwave observations to liquid water in the Antarctic snowpack, *The Cryosphere*, 16, 5061–5083, <https://doi.org/10.5194/tc-16-5061-2022>, 2022.

Rack, W. and Rott, H.: Pattern of retreat and disintegration of the Larsen B ice shelf, Antarctic Peninsula, *Annals of Glaciology*, 39, 505–510, <https://doi.org/10.3189/172756404781814005>, 2004.

710 705 Rignot, E., Mouginot, J., Scheuchl, B., Van Den Broeke, M., Van Wessem, M. J., and Morlighem, M.: Four decades of Antarctic Ice Sheet mass balance from 1979–2017, *Proceedings of the National Academy of Sciences*, 116, 1095–1103, <https://doi.org/10.1073/pnas.1812883116>, 2019.

Roeckner, E., Bäuml, G., Bonaventura, L., Brokopf, R., Esch, M., Giorgetta, M., Hagemann, S., Kirchner, I., Kornblueh, L., Manzini, E., Schlese, U., Schulzweida, U., and Tompkins, A.: The atmospheric general circulation model ECHAM 5. Part I: Model description, *Tech. Rep. Report 349*, Max Planck Institute for Meteorology, Hamburg, Germany, <https://hdl.handle.net/11858/00-001M-0000-0012-0144-5>, 2003.

715 Scambos, T., Fricker, H. A., Liu, C. C., Bohlander, J., Fastook, J., Sargent, A., Massom, R., and Wu, A. M.: Ice shelf disintegration by plate bending and hydro-fracture: Satellite observations and model results of the 2008 Wilkins Ice Shelf break-ups, *Earth and Planetary Science Letters*, 280, 51–60, <https://doi.org/10.1016/j.epsl.2008.12.027>, 2009.

720 Scambos, T. A., Bohlander, J. A., Shuman, C. A., and Skvarca, P.: Glacier acceleration and thinning after ice shelf collapse in the Larsen B embayment, *Antarctica, Geophysical Research Letters*, 31, <https://doi.org/10.1029/2004GL020670>, 2004.

Seroussi, H., Nowicki, S., Payne, A. J., Goelzer, H., Lipscomb, W. H., Abe Ouchi, A., Agosta, C., Albrecht, T., Asay-Davis, X., Barthel, A., et al.: ISMIP6 Antarctica: a multi-model ensemble of the Antarctic ice sheet evolution over the 21 st century, *The Cryosphere Discussions*, 2020, 1–54, <https://doi.org/10.5194/tc-14-3033-2020>, 2020.



720 Smith, R. S., Mathiot, P., Siahaan, A., Lee, V., Cornford, S. L., Gregory, J. M., Payne, A. J., Jenkins, A., Holland, P. R., Ridley, J. K., and Jones, C. G.: Coupling the U.K. Earth System Model to Dynamic Models of the Greenland and Antarctic Ice Sheets, *Journal of Advances in Modeling Earth Systems*, 13, e2021MS002520, <https://doi.org/10.1029/2021MS002520>, 2021.

Spiegel, J. J., Kingslake, J., Creyts, T., van Wessem, M., and Fricker, H. A.: Surface meltwater drainage and ponding on Amery Ice Shelf, East Antarctica, 1973–2019, *Journal of Glaciology*, 67, 985–998, <https://doi.org/10.1017/jog.2021.46>, 2021.

725 Tedesco, M., Doherty, S., Fettweis, X., Alexander, P., Jeyaratnam, J., and Stroeve, J.: The darkening of the Greenland ice sheet: trends, drivers, and projections (1981–2100), *The Cryosphere*, 10, 477–496, <https://doi.org/10.5194/tc-10-477-2016>, 2016.

The Firn Symposium team: Amory, C. et al.: Firn on ice sheets, *Nat. Rev. Earth. Environ.*, 5, 79–99, <https://doi.org/10.1038/s43017-023-00507-9>, 2024.

730 Torinesi, O., Fily, M., and Genthon, C.: Variability and trends of the summer melt period of Antarctic ice margins since 1980 from microwave sensors, *Journal of Climate*, 16, 1047–1060, [https://doi.org/10.1175/1520-0442\(2003\)016<1047:VATOTS>2.0.CO;2](https://doi.org/10.1175/1520-0442(2003)016<1047:VATOTS>2.0.CO;2), 2003.

van Kampenhout, L., Lenaerts, J. T., Lipscomb, W. H., Sacks, W. J., Lawrence, D. M., Slater, A. G., and van den Broeke, M. R.: Improving the representation of polar snow and firn in the Community Earth System Model, *Journal of Advances in Modeling Earth Systems*, 9, 2583–2600, <https://doi.org/10.1002/2017MS000988>, 2017.

735 van Kampenhout, L., Lenaerts, J. T., Lipscomb, W. H., Lhermitte, S., Noël, B., Vizcaíno, M., Sacks, W. J., and van den Broeke, M. R.: Present-day Greenland ice sheet climate and surface mass balance in CESM2, *Journal of Geophysical Research: Earth Surface*, 125, e2019JF005318, <https://doi.org/10.1029/2019JF005318>, 2020.

Van Wessem, J. M., Van De Berg, W. J., Noël, B. P., Van Meijgaard, E., Amory, C., Birnbaum, G., Jakobs, C. L., Krüger, K., Lenaerts, J. T., Lhermitte, S., et al.: Modelling the climate and surface mass balance of polar ice sheets using RACMO2–Part 2: Antarctica (1979–2016), *The Cryosphere*, 12, 1479–1498, <https://doi.org/10.5194/tc-12-1479-2018>, 2018.

740 Van Wessem, J. M., van den Broeke, M. R., Wouters, B., and Lhermitte, S.: Variable temperature thresholds of melt pond formation on Antarctic ice shelves, *Nature Climate Change*, 13, 161–166, <https://doi.org/10.1038/s41558-022-01577-1>, 2023.

Verro, K., Äijälä, C., Pirazzini, R., Dadic, R., Maure, D., van de Berg, W. J., Traversa, G., van Dalum, C. T., Uotila, P., Fettweis, X., Di Mauro, B., and Johansson, M.: How well do the regional atmospheric and oceanic models describe the Antarctic sea ice albedo?, <https://doi.org/10.5194/egusphere-2025-386>, EGUsphere preprint, 2025.

745 Wang, W., Shen, Y., Chen, Q., and Wang, F.: Unprecedented mass gain over the Antarctic ice sheet between 2021 and 2022 caused by large precipitation anomalies, *Environmental Research Letters*, 18, 124012, <https://doi.org/10.1088/1748-9326/ad0863>, 2023.

Willie, J., Favier, V., Jourdain, N., Kittel, C., Turton, J., Agosta, C., Gorodetskaya, I., Picard, G., Codron, F., Amory, C., et al.: Intense atmospheric rivers can weaken ice shelf stability at the Antarctic Peninsula, *Communications Earth & Environment*, 3, <https://doi.org/10.1038/s43247-022-00422-9>, 2022.